Journal of *Marine Science and Engineering*

MDPI

Article

Study on the Influence of 3D Printing Material Filling Patterns on Marine Photovoltaic Performance

Huiling Zhang [1], Shengqing Zeng [2], Yining Zhang [2], Sixing Guo [2], Huaxian Feng [2] and Dapeng Zhang [2,*]

[1] College of Ocean Engineering and Energy, Guangdong Ocean University, Zhanjiang 524088, China; zhanghl@gdou.edu.cn
[2] Ship and Maritime College, Guangdong Ocean University, Zhanjiang 524005, China
* Correspondence: zhangdapeng@gdou.edu.cn

Abstract

With the rapid development of offshore photovoltaic (PV) systems, PV support structures have become a critical component in offshore PV installations. The material properties of these structures significantly influence the safety and reliability of the entire system. 3D printing technology, leveraging its advantages such as rapid prototyping, complex structure manufacturing, and high material utilization, holds broad application prospects in the field of offshore PV. However, the infill pattern of 3D printing materials can significantly affect their mechanical properties. Marine PV systems require extremely high resistance to wave action, tensile strength, and torsional performance, while offshore PV support structures need sufficient compressive capacity. Therefore, this study aims to investigate how different infill patterns affect the compressive properties of 3D printed materials, thereby optimizing material selection and printing processes for offshore PV applications. Through experimental design, a variety of common infill patterns were selected. Universal testing machines and torsion testing machines were used to conduct systematic tests on compressive strength, elastic modulus, and compressive fracture strain. The results showed that different infill patterns have a significant impact on compressive properties, among which the honeycomb infill exhibited the best overall mechanical performance, effectively enhancing load-bearing capacity and stability. Based on the experimental results, appropriate infill configurations and material combinations for different components of offshore PV systems were proposed. The feasibility of optimizing 3D printing processes to improve the overall performance of offshore PV structures was further explored. The findings of this study not only provide a theoretical basis for material selection and process optimization in 3D printing for offshore PV systems but also offer important references for promoting the application of 3D printing technology in this field.

Keywords: 3D printing materials; infill patterns; compressive properties; marine photovoltaics

check for updates

Academic Editor: Bang-Fuh Chen

Received: 11 November 2025
Revised: 12 December 2025
Accepted: 12 December 2025
Published: 14 December 2025

Citation: Zhang, H.; Zeng, S.; Zhang, Y.; Guo, S.; Feng, H.; Zhang, D. Study on the Influence of 3D Printing Material Filling Patterns on Marine Photovoltaic Performance. *J. Mar. Sci. Eng.* **2025**, *13*, 2373. https://doi.org/10.3390/jmse13122373

Copyright: © 2025 by the authors. Licensee MDPI, Basel, Switzerland. This article is an open access article distributed under the terms and conditions of the Creative Commons Attribution (CC BY) license (https://creativecommons.org/licenses/by/4.0/).

1. Introduction

The rapid advancement of technology, industrialization, and population growth has led to an ongoing increase in global energy demand, with projections suggesting a substantial rise by 2040 [1]. Non-renewable fossil fuels, however, encounter several challenges, including limited reserves [2], environmental pollution, and greenhouse gas emissions, particularly carbon dioxide. These issues contribute to adverse weather events and environmental concerns such as global warming and acid rain [3,4]. Consequently, there is an urgent need to investigate renewable and environmentally sustainable energy solutions.

Various sources, including solar [5], hydro [6], geothermal [7], biomass [8], and wind [9] energy, have been proposed and extensively studied. Among these, solar energy emerges as a significant and promising alternative. Current floating photovoltaics (FPV) can be classified based on their deployment environment into three categories: floating PV, above-water PV, and submerged PV [10], as shown in Figure 1.

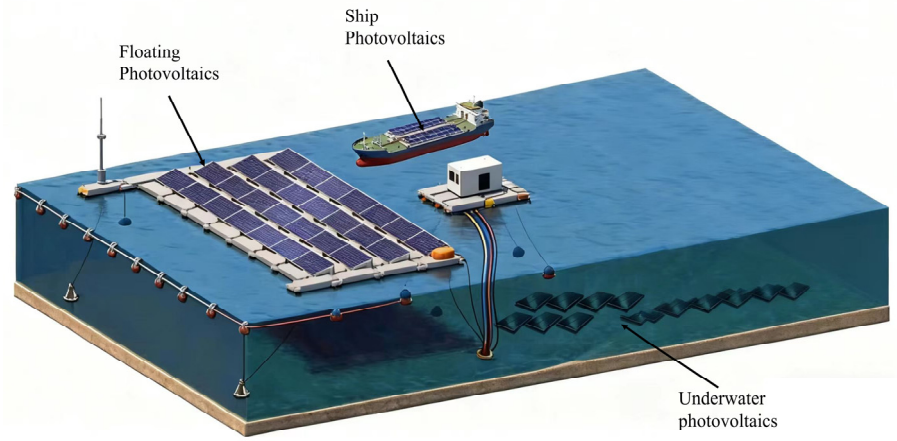


Figure 1. Different types of marine photovoltaics.

FPV denotes photovoltaic systems installed on water surfaces. These systems generally consist of floats, support structures, mooring systems, photovoltaic modules, electronic components, and tracking systems. Depending on the installation environments and system designs, above-water photovoltaic systems can be classified into fixed-pile PV systems and those specifically engineered for large ocean-going vessels. To mitigate environmental impacts on the panels, submerged underwater PV (UPV) systems have been developed. This approach stabilizes panel temperatures, streamlines the structure of photovoltaic inverters, and removes the necessity for additional cleaning equipment [10–12]. In marine environments, the support structure is essential for maintaining panels at a safe elevation above sea level [13]. Mooring systems secure the entire floating photovoltaic (FPV) array against environmental loads, limiting the equipment's movement to ensure stability and safety [14]. This configuration prevents the FPV system from capsizing or drifting away [15]. In freshwater FPV projects, synthetic fiber ropes, elastic rubber ropes, or combinations of both materials are commonly used [16]. Conversely, mooring lines for offshore floating platforms are generally made of steel cables or steel wire ropes [17]. Marine Photovoltaic (MPV) systems are exposed to severe environmental conditions, including storms and waves, which render them vulnerable to natural disasters that can result in equipment damage and interruptions in power generation [18]. As a result, MPV supports must possess the capability to endure such adverse conditions. Various materials exhibit unique properties, and the necessary characteristics of marine PV support structures differ according to the type of project and the surrounding environmental conditions [19–23]. Nonetheless, the high costs associated with physical testing of marine PV systems restrict research in this field. The emergence of 3D printing technology offers a cost-effective alternative. This approach enables the fabrication of diverse components using multiple materials, specifically designed to meet particular requirements. Consequently, it has facilitated experimental exploration in the field of marine photovoltaic research [24,25]. In the studies mentioned above and in most existing research, traditional steel materials have been employed for marine photovoltaics. The high cost of these materials significantly elevates both experimental and construction expenses in this domain. To address the financial challenges associated with research and practical implementation, this paper proposes the use of 3D printing technology with polylactic acid (PLA) as the material for fabricating components

necessary for marine photovoltaics, thereby reducing overall costs. To assess the feasibility of PLA for marine photovoltaic components, this study printed standard compression test specimens from PLA and conducted strength testing. This material substitution has the potential to substantially lower both research and construction costs in this field. To enhance the mechanical properties of PLA for industrial applications, techniques such as plasticization, blending, and other modifications have been proposed to improve its degradability, mechanical strength, and physical and biological properties. Several researchers have documented methods for modifying PLA's hydrophilicity, degradability, and elongation at break. Blends of PLA with various synthetic and biopolymers have been developed to enhance its properties [26–28]. Reports suggest that the combination of PLA with substances like collagen improves its performance relative to the pure polymer, resulting in enhanced toughness, modulus, impact strength, and thermal stability [29,30]. These studies demonstrate that PLA, through ongoing research and optimization, has attained conditions suitable for complex engineering environments.

This paper begins by detailing our printing tools and specimen materials in Section 2, outlining the various parameters of the specimens, including printing angle, printing method, and infill density, as well as the procedures employed in conducting experiments on different specimens. Section 3 then analyzes the experimental data obtained and compares the conclusions of this study with existing research. Finally, the conclusion summarizes the research findings.

2. Experiment

2.1. Experimental Equipment

This experiment utilized the Bambu Lab's P1S 3D printer (Bambu Lab, Shenzhen, China) with polylactic acid (PLA) as the printing material to prepare samples. PLA has a melting point range of 190 to 220 °C and exhibits excellent printability and mechanical properties (as shown in Figure 2). Its eco-friendly and economical characteristics make it an ideal choice for this study. Default parameter settings were employed throughout the printing process: layer thickness of 0.2 mm, print speed of 60 mm/s, nozzle temperature of 210 °C, and heated bed temperature of 60 °C. Printing proceeded along the X-axis with material extrusion perpendicular to the XY plane. Material was kept dry during printing to ensure consistent print quality. The printer achieves positioning accuracy of ±0.02 mm along the XYZ axes. This means that under optimal settings, dimensional deviations between printed models and design specifications are typically controlled within 0.02 mm.

Compression tests were conducted using an ETM series electronic universal testing machine (WANCE, Shenzhen, Chian) with a maximum load capacity of 30 kN and an accuracy of ±0.5%. This testing machine is equipped with a compression fixture and a displacement transducer, enabling precise measurement of the load–displacement curve during the compression process. The data acquisition system records test data in real time and subsequently analyzes and processes it through the accompanying software.

2.2. Design of Experimental Parts

Referencing Jiang's research [31], PLA material was employed to print experimental specimens in this study. Different infill patterns, infill densities, and printing angles were also utilized for specimen printing.

The initial group of controlled experiments was structured to include three infill patterns—honeycomb, spiral, and linear infill—as depicted in Figure 3. Additionally, four infill ratios (25%, 35%, 50%, and 75%) were employed to systematically examine the effects of both infill patterns and infill ratios on the compression properties of 3D printed

specimens. The specific design is as follows: the honeycomb infill utilizes a hexagonal cell structure, with filling ratios of 25%, 35%, 50%, and 75% achieved by adjusting the density of the hexagonal cells; the spiral infill employs a helical path design, with the same filling ratios controlled by varying the sparseness of the helical paths; and the linear infill consists of parallel linear paths, with filling ratios of 25%, 35%, 50%, and 75% realized by modifying the spacing between the linear paths. Multiple sets of standard compression specimens were printed for each combination of infill pattern and infill ratio. Based on international standards [32], we developed a model for compressed specimens. The dimensions and shape of the specimens were rigorously designed to meet the requirements of standard compression testing, as shown in Figure 4.

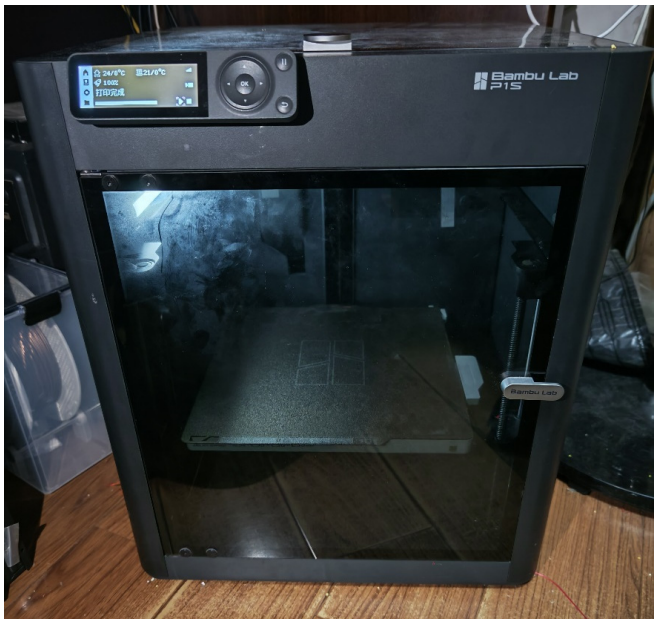


Figure 2. Printer used to print the specimen.

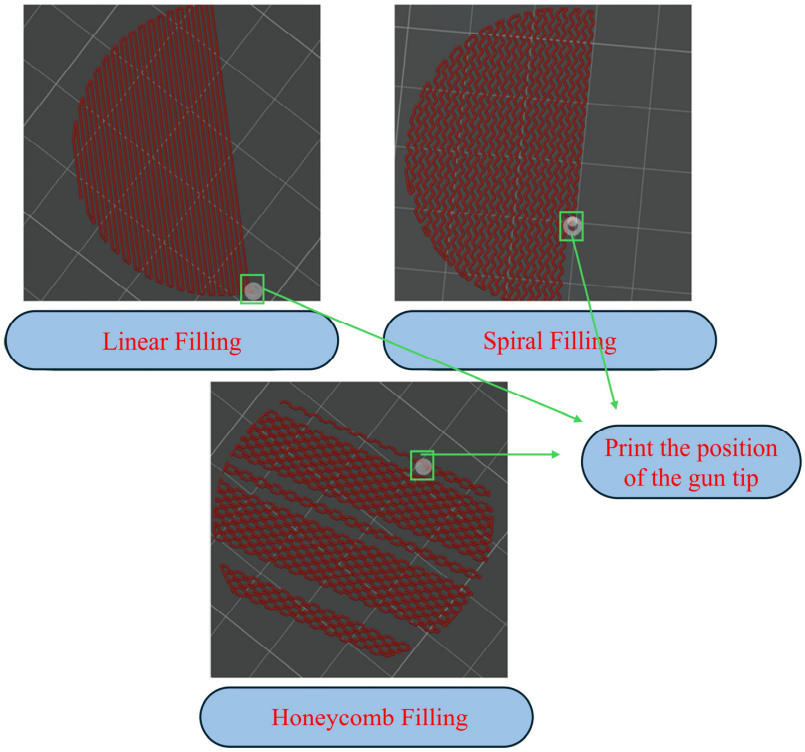


Figure 3. Three different fill styles.

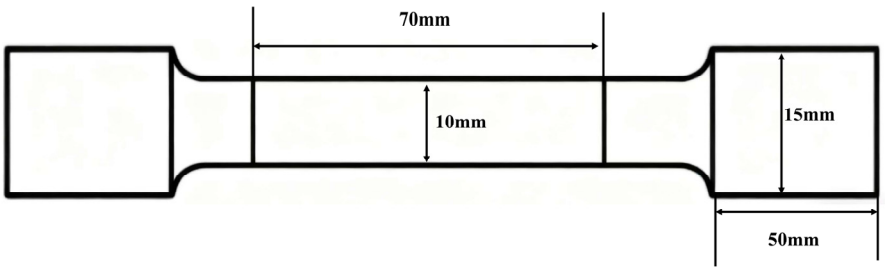


Figure 4. Component Dimensions and Styles.

This approach ensured the accuracy and comparability of the experimental results. The experimental design allowed for a comprehensive evaluation of the combined effects of various filling patterns and filling ratios on the compressive performance of the specimens, thereby providing reliable data to support subsequent analyses and optimizations of mechanical properties.

The second set of control tests was derived from the initial experiments. Each filling form—honeycomb, spiral, and linear—was printed according to the printing directions of 0°, 15°, 30°, 45°, 60°, 75°, and 90°. One specimen was printed for each group while maintaining consistent conditions across all tests. The objective of these experiments was to examine the effects of printing direction on the compressive properties of the materials, specifically focusing on the maximum compressive stress, modulus of elasticity, and damage modes of the specimens under varying printing orientations. It is anticipated that a significant difference in compressive properties will exist between specimens printed at 0° and those printed at 90°. Specimens printed at 0° are expected to demonstrate higher compressive strength and stiffness, whereas those printed at 90° may exhibit more extensive compressive damage. Honeycomb infill and spiral infill exhibit smaller variations in performance across different print orientations, whereas linear infill is more significantly influenced by print orientation.

This tilt angle refers to the angle between the sample axis and the print bed, as shown in Figure 5 below, representing a straight line forming an angle with the surface. This angle is called the print tilt angle or the sample tilt angle.

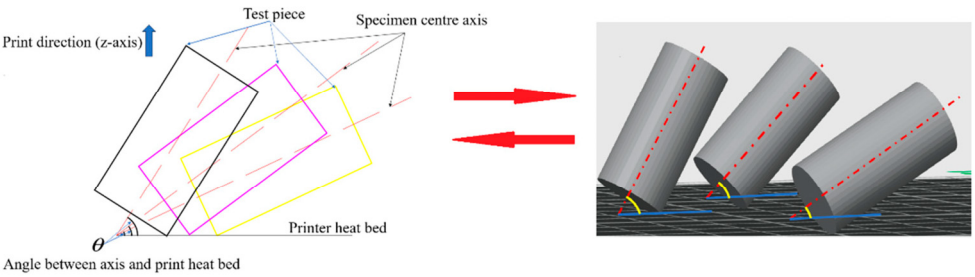


Figure 5. Print the diagram of the tilt angle. The red arrows indicate the transition between the 3D and 2D schematics, and the blue arrows indicate the positive direction of the Z-axis.

This experiment comprehensively evaluated the impact of printing direction on the compressive properties of 3D-printed materials, providing reliable data for optimizing marine photovoltaic designs. In addition, it lays the foundation for further optimization of 3D printing process parameters, thereby enhancing the performance and reliability of marine photovoltaics. Future research should explore the interactions between printing direction and other process parameters to further advance the application and development of 3D printing technology in the field of marine photovoltaics.

2.3. Experimental Process and Data Processing

The test was conducted at room temperature (25 °C) under normal environmental conditions with the specimen kept dry is shown Figure 6. Prior to starting the test, the lower platform was leveled to ensure horizontal alignment. After confirming platform levelness, the specimen was placed into the compression fixture of the universal testing machine. The compression device was then activated, applying a compressive load at a rate of 2 mm per minute until specimen failure. The machine was stopped upon specimen failure. Load–displacement data is recorded in real time throughout the test, while the specimen's deformation and damage patterns are observed.

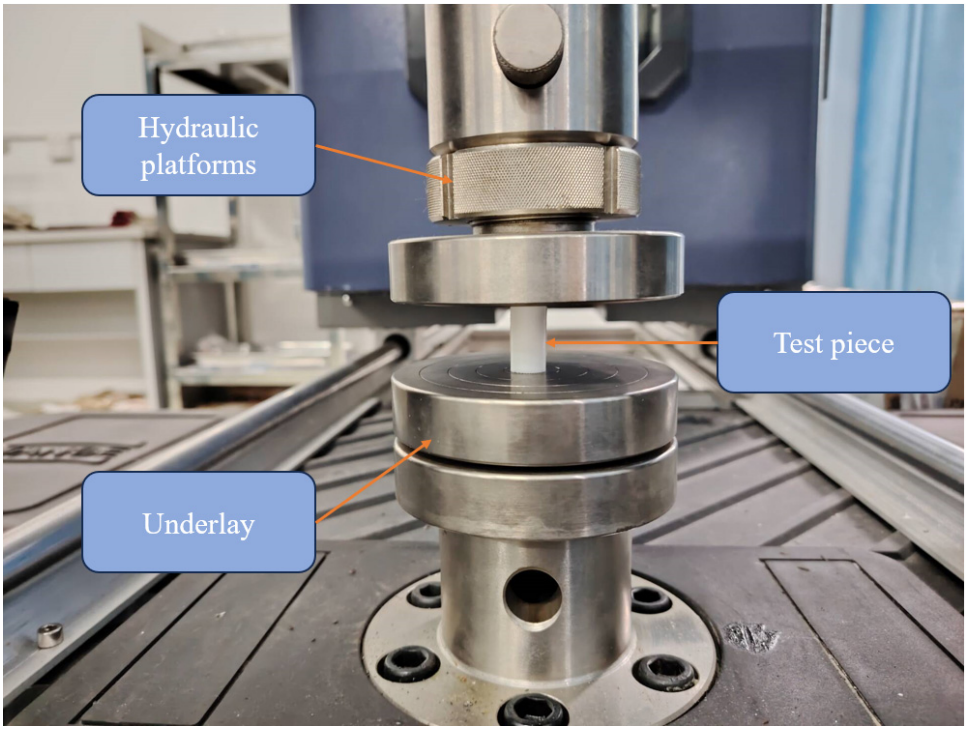


Figure 6. Experimental apparatus.

The test data were collected via the data acquisition system of the universal material testing machine, encompassing key parameters such as maximum compressive strength, modulus of elasticity, and damage mode. Statistical analysis of the data was performed using Origin software 2024 to generate load–displacement curves and to calculate the average mechanical properties for various filling forms and filling ratios.

This study employs the previously mentioned experimental approaches to investigate three key influencing factors of the components. The first factor analyzed is the filling structure, which includes a total of three variables. The second factor is the filling rate, comprising four variables. The third factor relates to the specimen inclination angle, totaling seven variables, as shown in Table 1.

Table 1. Study variables.

Research Factors							
Filling structure	Honeycomb			Spiral		Linear	
Filling rate	25%		35%		50%		75%
Specimen tilt angle	0°	15°	30°	45	60°	75°	90°

2.4. Theoretical Equation

Hooke's Law: Within the elastic range, the relationship between stress (σ) and strain (ε) can be expressed by the following Equation (1), where $\boldsymbol{E}$ is the material's modulus of elasticity, F is the applied force, and $\boldsymbol{A}$ is the cross-sectional area in Equation (2).

$$\sigma = E\varepsilon \tag{1}$$

$$\sigma = \frac{F}{A} \tag{2}$$

$$\varepsilon = \frac{\Delta L}{L_0}, \quad v = -\frac{\varepsilon_{lat}}{\varepsilon_{lang}}, W = \frac{1}{2}\sigma\varepsilon \tag{3}$$

In Equation (3), ΔL denotes the change in length of the specimen when loaded, and L_0 is the original length of the specimen. v denotes Poisson's ratio, which describes the ratio of the strain in one direction to the strain perpendicular to that direction, and ε_{lat} denotes transverse strain denotes longitudinal strain. ε_{long} The stored energy density is denoted as W.

Consider the microelementary hexahedron in one of the specimens, and let it have three main directions of stress components in xyz coordinate system: positive stress $\sigma_x, \sigma_y, \sigma_z$ and shear stress component $\tau_{xy}, \tau_{xz}, \tau_{yz}$; therefore, the stress state of the microelementary hexahedron can be expressed by the following stress tensor as the following Equation (4):

$$\sigma = \begin{pmatrix} \sigma_x & \tau_{xy} & \tau_{xz} \\ \tau_{xy} & \sigma_y & \tau_{yz} \\ \tau_{xz} & \tau_{yz} & \sigma_z \end{pmatrix} \tag{4}$$

The maximum stress can be obtained from the characteristic Equation (5), where λ is the principal stress and I is the identity matrix.

$$d(\sigma - \lambda I) = 0 d = \begin{pmatrix} \sigma_x - \lambda & \tau_{xy} & \tau_{xz} \\ \tau_{xy} & \sigma_y - \lambda & \tau_{yz} \\ \tau_{xz} & \tau_{yz} & \sigma_z - \lambda \end{pmatrix} \tag{5}$$

Yao et al. pointed out that 3D printing is stacked layer by layer, which can be considered transversely isotropic in the plane of any layer, and provided the elastic intrinsic relationship of the material [33], as shown in Equation (6) below.

$$\begin{bmatrix} \varepsilon_1 \\ \varepsilon_2 \\ \varepsilon_3 \\ \varepsilon_4 \\ \varepsilon_5 \\ \varepsilon_6 \end{bmatrix} = \begin{bmatrix} S_{11} & S_{12} & S_{12} & 0 & 0 & 0 \\ S_{12} & S_{22} & S_{23} & 0 & 0 & 0 \\ S_{12} & S_{23} & S_{22} & 0 & 0 & 0 \\ 0 & 0 & 0 & 2(S_{22} - S_{23}) & 0 & 0 \\ 0 & 0 & 0 & 0 & S_{56} & 0 \\ 0 & 0 & 0 & 0 & 0 & S_{65} \end{bmatrix} \begin{bmatrix} \sigma_1 \\ \sigma_2 \\ \sigma_3 \\ \sigma_4 \\ \sigma_5 \\ \sigma_6 \end{bmatrix} \tag{6}$$

For the plane stress state, then we have $\sigma_3 = 0$, $\tau_{23} = \sigma_4 = 0$, $\tau_{31} = \sigma_5 = 0$; the eigenstructure matrix can be written as Equation (7).

$$\begin{bmatrix} \varepsilon_1 \\ \varepsilon_2 \\ \gamma_{12} \end{bmatrix} = \begin{bmatrix} S_{11} & S_{12} & 0 \\ S_{12} & S_{22} & 0 \\ 0 & 0 & S_{55} \end{bmatrix} \begin{bmatrix} \sigma_1 \\ \sigma_2 \\ \tau_{12} \end{bmatrix} \gamma_{\mathrm{al}} = \gamma_{\mathrm{al}} = 0, \varepsilon_3 = S_{13}\sigma_1 + S_{23}\sigma_2 \tag{7}$$

where the E_1, E_2 engineering constants are Young's modulus; Poisson's ratio, ν_{12}, $\nu_{21}G_{12}$; and shear modulus. The matrix of four elastic constants can be expressed as Equation (8):

$$\begin{aligned} S_{11} &= \frac{1}{E_1} \\ S_{22} &= \frac{1}{E_2} \\ S_{56} &= \frac{1}{G_{12}} \\ S_{12} &= -\frac{\nu_{21}}{E_1} = -\frac{\nu_{12}}{E_2} \end{aligned} \tag{8}$$

The volume of the model we created in SolidWorks 2024 is referred to as the model volume, denoted by V. The fill volume represents the portion of the model volume that has been hollowed out, with the remaining volume classified as the fill volume, which directly indicates the amount of material used. The filling rate is defined as the ratio of the total fill volume to the model volume, multiplied by 100%. The specimen is constructed layer by layer, where V_i represents the fill volume of the i layer, M_i denotes the model volume of the i layer, S_i refers to the filling cross-sectional area of the i layer, and A_i signifies the model cross-sectional area of the i layer. The filling rate is represented by ρ, the height of the layer is indicated by h, and the extruded material of the 3D printer for the i layer is expressed as L_i. The total length of the filament is also denoted as L_i, while α represents the width of the extruded filament, determined by the print nozzle. In summary, we can derive the definition in Equation (9) for the fill rate.

$$\rho = \left(\frac{\sum V_i}{V}\right) \times 100\% \tag{9}$$

$$V_i = S_i \cdot h,\ M_i = A_i \cdot h \tag{10}$$

$$\sum V_i = \sum S_i \cdot h, \sum M_i = \sum A_i \cdot h \tag{11}$$

$$S_i = L_\mathrm{i} \cdot \alpha \tag{12}$$

$$\rho = \frac{\sum L_i \cdot \alpha}{\sum A_i} \times 100\% \tag{13}$$

As indicated in the combined formula, Formula (14), let a, m and s represent the number of variables for the four research factors: filling structure, filling rate, specimen inclination angle, and experimental load, respectively. The total number of specimens, denoted as P in Equation (15), is established with $b = n = f = 1$ using the control variable method.

$$C_x^y = \frac{x!}{y!(x-y)!} \tag{14}$$

$$P = C_a^b C_m^n C_s^f \tag{15}$$

Substituting the data $b = n = f = 1$, $a = 3$, $m = 4$, $s = 7$ to find the total number of specimens, $P = 84$, we get 84 independent data points. The distribution of data points and the number of experiments conducted for each data point are shown in Table 2.

Table 2. Distribution of Data Points and Number of Experiments.

Filling Structure	Filling Rate	Specimen Tilt Angle	Number of Samples	Number of Experiments
Honeycomb	25%	0°/15°/30°/45°/60°/75°/90°	7	12
Honeycomb	35%	0°/15°/30°/45°/60°/75°/90°	7	12

Table 2. *Cont.*

Filling Structure	Filling Rate	Specimen Tilt Angle	Number of Samples	Number of Experiments
Honeycomb	50%	0°/15°/30°/45°/60°/75°/90°	7	12
Honeycomb	75%	0°/15°/30°/45°/60°/75°/90°	7	12
Spiral	25–75% (Consistent with the honeycomb structure	0°/15°/30°/45°/60°/75°/90°	28	12
Linear	25–75% (Consistent with the honeycomb structure	0°/15°/30°/45°/60°/75°/90°	28	12

3. Results and Discussion

3.1. Data Analysis

The compression testing machine we use is the ETM series electronic universal testing machine. Before commencing the experiment, the lower platform must be leveled to ensure horizontal alignment; the upper platform compresses the test specimen downward at a rate of 2 mm per minute. The force–compression displacement curve exhibits only one form, as shown in Figure 7; the initial stage involves force increasing the compression within the specimen, enabling it to withstand a rapid rise in pressure after reaching a certain pressure value during the slow increase phase. At both ends of the platform where force is applied, the specimen's constraints prevent deformation; the cross-section in the specimen's center, subjected to increasing pressure, continues to thicken, and its load-bearing capacity increases accordingly. When deformation approaches 5 mm, the test specimen fails, and the experiment is terminated. The damaged specimen is shown in Figure 8.

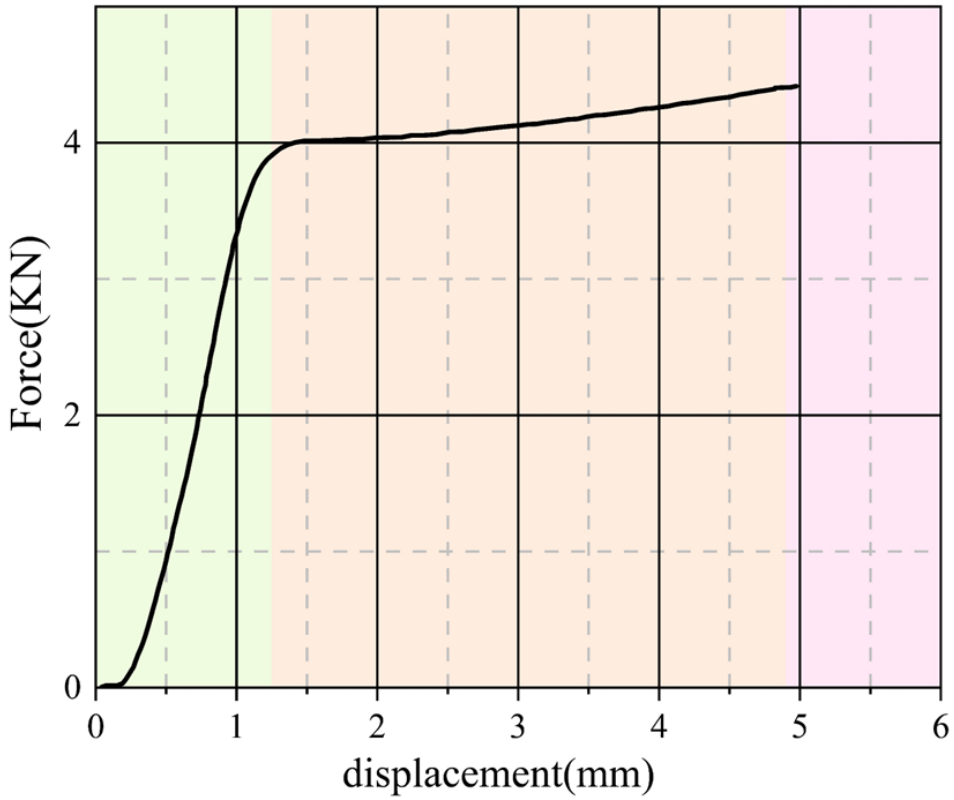


Figure 7. Stress–strain curve of the compressed specimen. The green area represents the linear stage, the orange area represents the yielding stage, and the pink area represents the fracture stage.

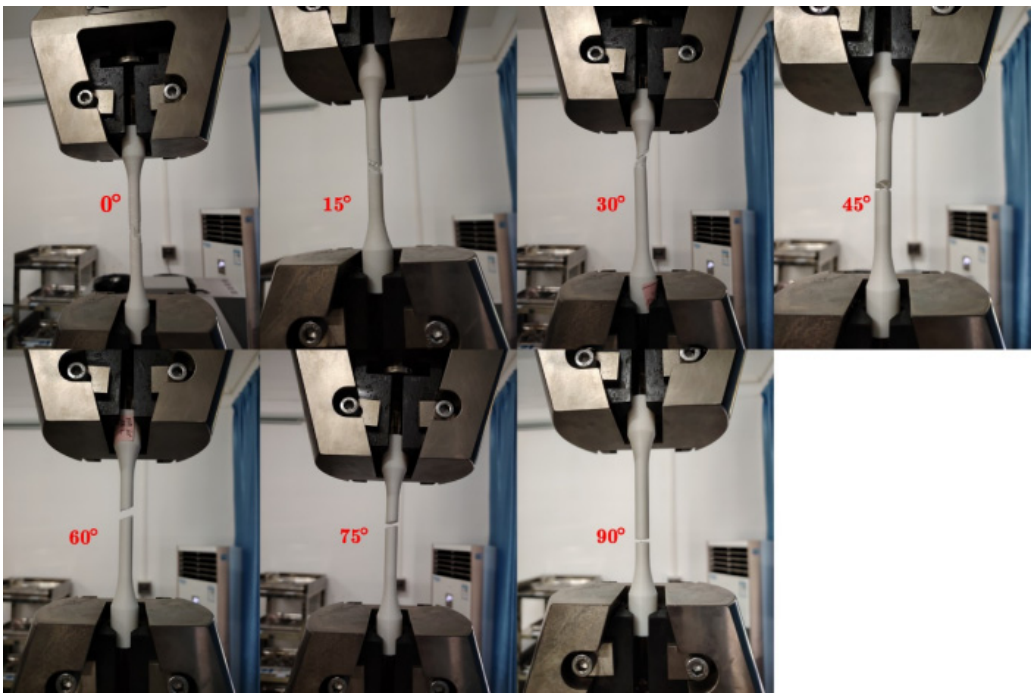


Figure 8. Picture of the test specimen damaged due to compression.

Analysis of experimental data indicates a significant correlation between the mechanical properties of various filler structures and their topological design. Under consistent filling ratios, the honeycomb filling structure exhibits optimal compressive performance due to its biomimetic hexagonal cell design, as illustrated in Figure 9. When the filling rate increases from 25% to 50%, the maximum compressive stress rises from 3.304 kN to 4.818 kN, representing a 45.8% increase. This enhancement reflects the ability of hexagonal cells to effectively delay material damage mechanisms by uniformly distributing stress. A stress relaxation of 2.3% (from 4.818 kN to 4.708 kN) occurs once the filling rate reaches 50%. According to Formula (4), hexagonal pressure is determined jointly by three directions. As filling increases, differential units in each direction acquire more material, thereby enhancing their compressive performance and effectively mitigating structural damage. A similar stress shrinkage of 2.3% (from 4.818 kN to 4.708 kN) is observed after surpassing the 50% filling rate. The honeycomb filling employs a biomimetic hexagonal cell structure whose topological design inherently possesses "trisubstructural stress balance" characteristics. This aligns with the synergistic interaction of the three stress components as defined by stress tensor Equation (4). When the filling rate increases from 25% to 50%, the wall thickness of hexagonal cells grows and cell density rises. This allows stress to be uniformly distributed throughout the structure via the hexagonal edges under compression, preventing localized stress concentration. Simultaneously, according to Hooke's law (Equation (1)), the material's elastic modulus is positively correlated with stress transfer efficiency. The increased packing ratio means more "differential elements" bear the load and a higher proportion of material is engaged. Each element can more effectively share the load, delaying the damage progression of "elastic deformation $\longrightarrow$ plastic deformation $\longrightarrow$ fracture". This ultimately manifests as a significant increase in compressive stress. The printing angle affects the degree of fiber interlacing between layers. When printed at 75°, the cross-angle of fibers in the honeycomb structure approaches 45°, enhancing the structure's shear resistance and thus achieving the highest maximum compressive stress.

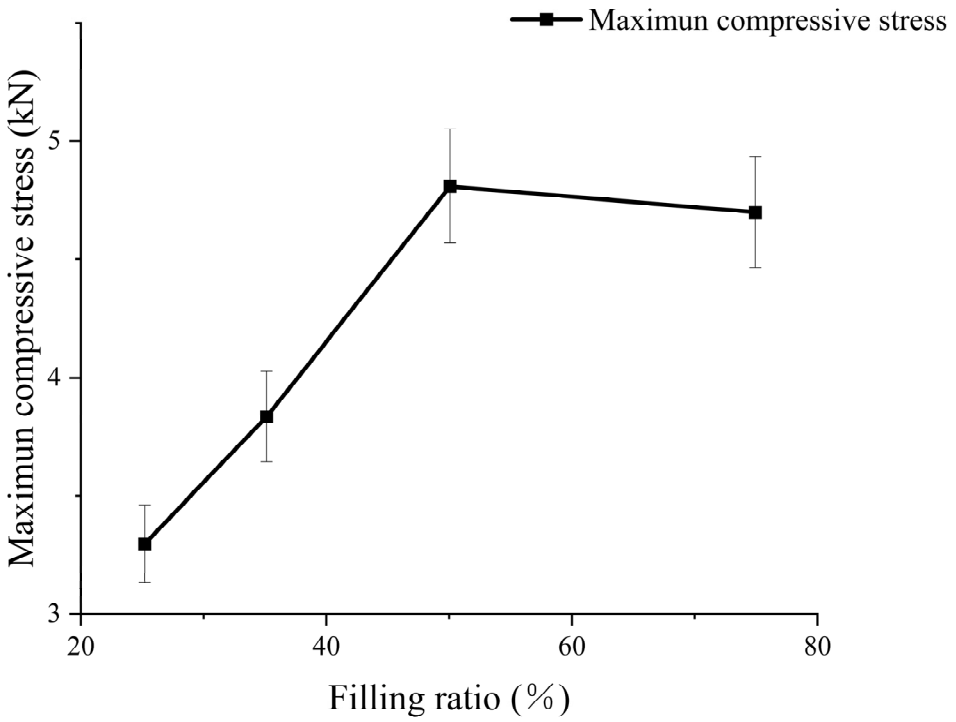


Figure 9. Trend of maximum compressive stress of honeycomb-filled specimen with increasing filling ratio.

As shown in Figure 10, the compressive curve (3.078 ⟶ 3.966 kN) of the helical-filled structure exhibits a honeycomb-like decay trend. The observed 32.8% gain in axial strength, relative to straight-line filling, at 50% filling supports the geometrical advantage of the helical structure in resisting bending-torsional coupling loads. However, the 5.4% stress decay at 75% filling indicates a threshold effect of helical spacing on plastic flow. The helical path design with spiral filling endows it with "bending–torsion coupled load resistance capability"—under compression, the spiral's intertwined structure partially converts axial pressure into tangential stress, dispersing concentrated loads from a single direction. When the filling rate increases from 25% to 50%, the pitch of the spiral path decreases and the linear density increases, enhancing the structure's "spatial entanglement stiffness". This creates a more continuous load transfer path, resulting in a sustained increase in axial compressive stress. Compared to linear filling, the spiral structure exhibits tighter interlayer bonding (with no distinct parallel interfaces), resulting in weaker stress concentration effects. Consequently, at 50% filling rate, compressive stress is 32.8% higher than in linear filling.

As shown in Figure 11, the low mechanical efficiency of the linearly filled body, which is 27.3% lower than that of the honeycomb structure at 50% filling, highlights an inherent flaw in the anisotropic design. This flaw arises from the stress-concentration effect at the interlayer interfaces, which complicates the ability to surpass the 50% filling threshold of the honeycomb structure, even under the strong constraint of 75% filling (3.39 kN). The quantitative results of these structure-function relationships offer a critical parameter optimization space for the additive manufacturing-based reverse design of porous materials. Linear filling employs a parallel straight-line path design, forming "parallel interlayer interfaces" after 3D printing. This structure exhibits unidirectional load transfer pathways, effectively transmitting stress only along the linear path direction, while interlayer bonding perpendicular to the path direction is extremely weak. According to the "stress transfer principle for anisotropic materials" in materials mechanics, the transverse (perpendicular to the straight path) elastic modulus of linear structures is significantly

lower than the longitudinal modulus. Under compression, stress tends to accumulate at the interlayer interfaces, creating a "potential shear failure risk". Even with increased fill density, interlayer defects persist, resulting in inherently inadequate mechanical efficiency.

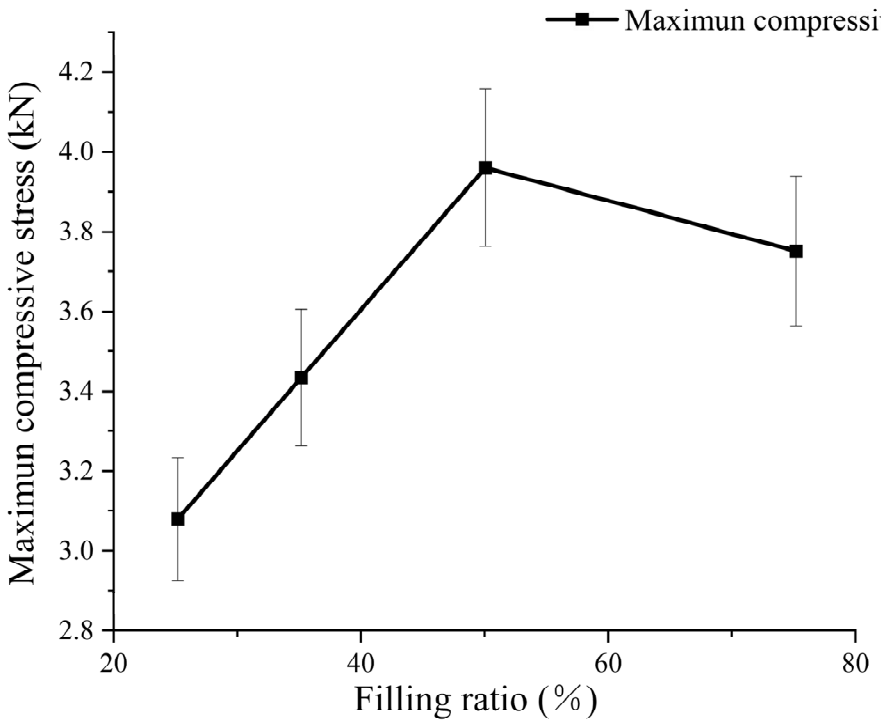


Figure 10. Trend of maximum compressive stress of spiral-filled specimen with increasing filling ratio.

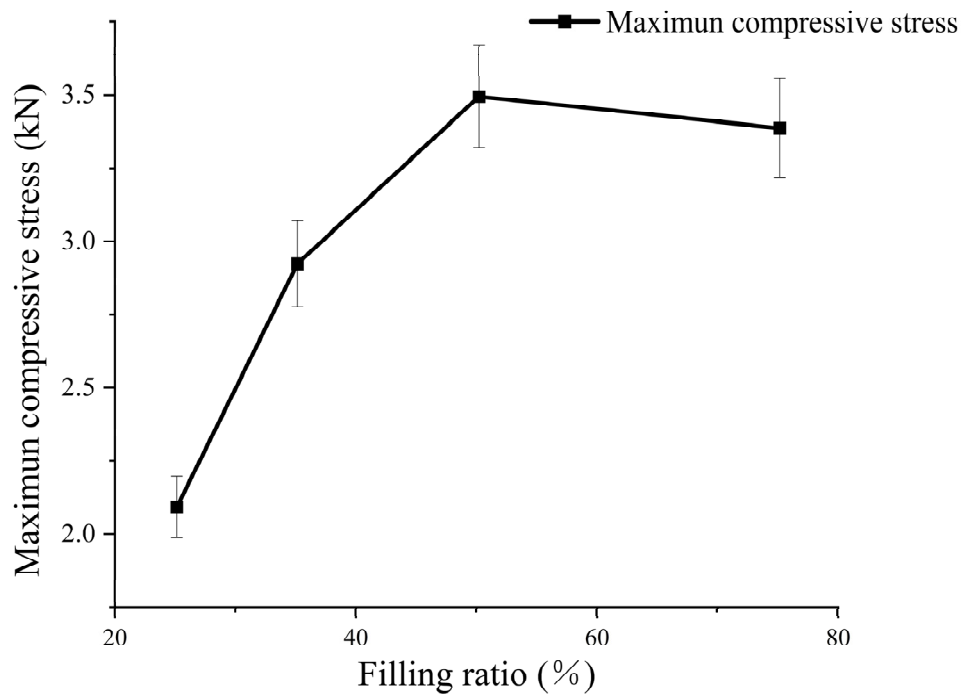


Figure 11. Trend of maximum compressive stress of linearly filled specimens with increasing filling ratio.

As shown in Figures 12–14. By analyzing the maximum compressive stress data of different filling forms (honeycomb, spiral and linear filling) at different printing angles (0°, 15°, 30°, 45°, 60°, 75°, 90°), it can be found that the influence of printing angle on

the compression performance of the specimen shows a certain regularity. In general, the maximum compressive stress with the change in printing angle usually shows a decreasing and then increasing trend; 15° or 30° is usually the lowest point of performance, while 0° or 90° is the highest point of performance. Specifically, the honeycomb infill specimen has the best performance at 75° or 90° printing direction, for example, the maximum compressive stress of 75% honeycomb infill specimen reaches 5.095 kN at 75°, which is the highest value among all the specimens, indicating that the honeycomb infill has excellent load-bearing capacity and impact resistance at high angle printing direction; while the spiral infill and linear infill specimens have better performance at 0° or 90° printing direction. For example, the maximum compressive stress of the 75% spiral-filled specimen at 90° was 4.38 kN, and that of the 75% linear-filled specimen at 90° was 4.061 kN, indicating that the spiral-filled and linear-filled specimens have high compressive performance under these printing directions. In addition, from the above three graphs, it can be seen once again that the compressive properties of the specimens generally show an upward trend with the increase in the filling ratio, e.g., the maximum compressive stress of the specimens with a 75% filling ratio is significantly higher than that of the specimens with a 25% filling ratio in most of the printing orientations, which indicates that a high filling ratio can effectively increase the load-carrying capacity of the material. However, in some printing directions (e.g., 15°and 30°), the increase in filling ratio has limited effect on the compression performance, e.g., the maximum compressive stress of 25% cellular filled specimen at 15°is 1.989 kN, while that of 75% cellular filled specimen at 15°is 4.988 kN, which is improved but still lower than that of the performance in other printing directions. Taken together, the honeycomb-filled specimen performs best under the high-angle printing direction (75° or 90°), which is suitable for application scenarios that require high load-bearing capacity and impact resistance; the spiral-filled and linear-filled specimens perform better under the 0° or 90° printing direction, which is suitable for parts requiring torsional resistance and lightweight design.

Due to the "multi-directional stress adaptability" of the hexagonal structure in honeycombs, during high-angle printing, the edges of hexagonal cells form obtuse angles with the load direction. This allows stress dispersion through elastic deformation of the edges. Furthermore, when printing at 90°, the stacking direction aligns parallel to the vertical edges of the hexagons. This maximizes the "effective stress-bearing length" of the load-bearing cells, resulting in the highest load-carrying capacity. At the same time, when the specimen is subjected to compression, the deposition direction of PLA aligns with the printing tilt angle of the specimen. At 0° printing, the layers bond along the X-axis, and at 90°, they bond along the Y-axis. Since the longitudinal strength of PLA is 20–30% higher than the transverse strength, the performance of the specimens printed at 0° and 90° is better than at intermediate angles.

The winding direction of the spiral structure is directly related to the printing angle. At 0° printing, the spiral winds axially, directly resisting axial pressure. At 90° printing, the spiral winds radially, forming a "ring-shaped load-bearing structure" that enhances the synergistic effect of torsion and compression resistance. When printing at an oblique angle, the winding direction of the spiral becomes misaligned with the load direction, disrupting the stress transfer path and resulting in reduced performance.

When the linear path aligns with the print angle, the path direction is either parallel (0°) or perpendicular (90°) to the load direction. When parallel, stress transfers directly along the path; when perpendicular, the path forms a "transverse support" that prevents layer delamination. During angled printing, the path forms an acute angle with the load direction, concentrating stress at path intersections and resulting in the lowest performance.

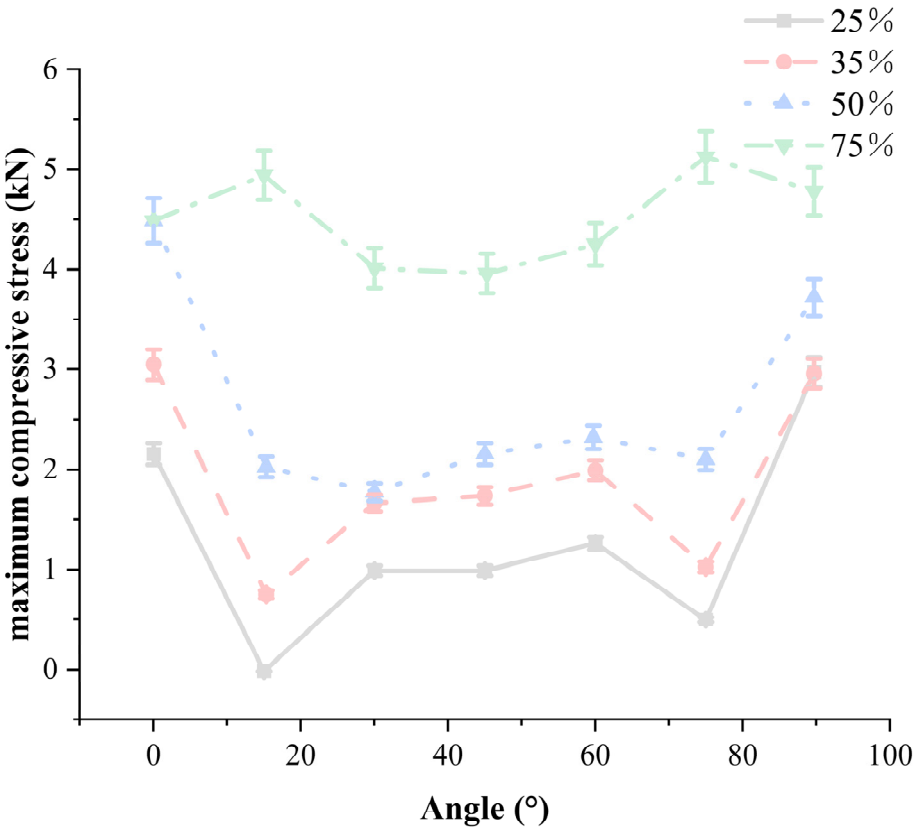


Figure 12. Variation in maximum compressive stress with printing angle for honeycomb-filled specimens with different filling ratios.

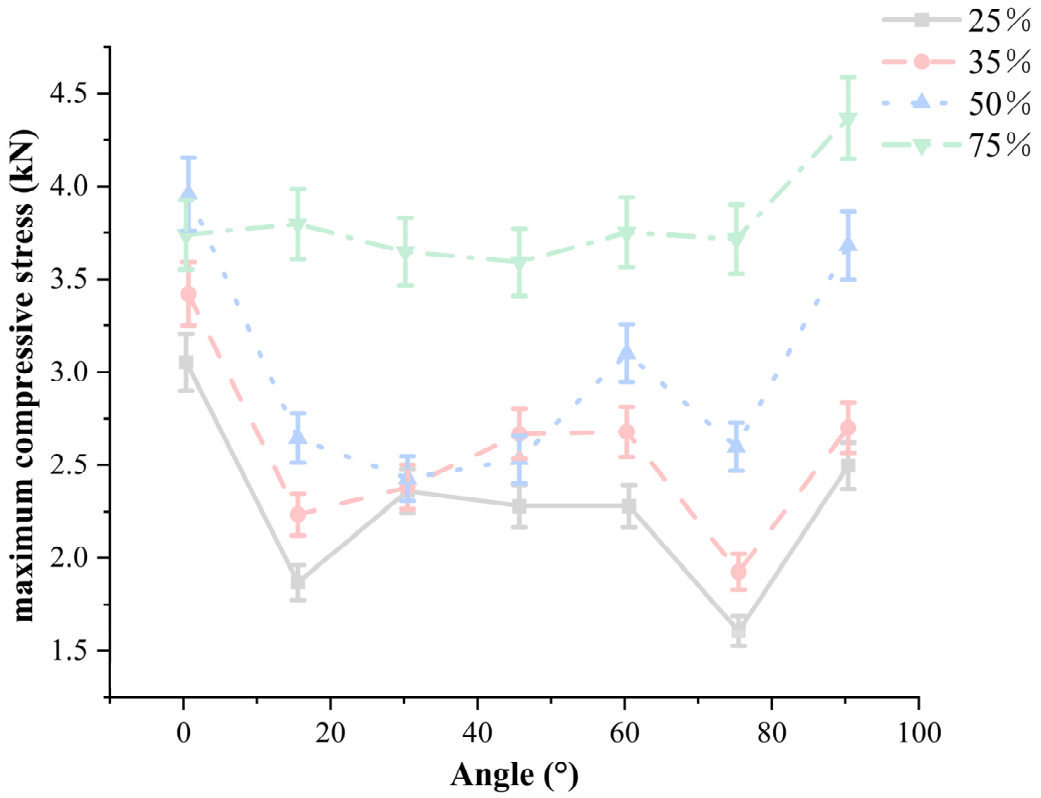


Figure 13. Variation in maximum compressive stress with printing angle for different filling ratios of spiral-filled specimens.

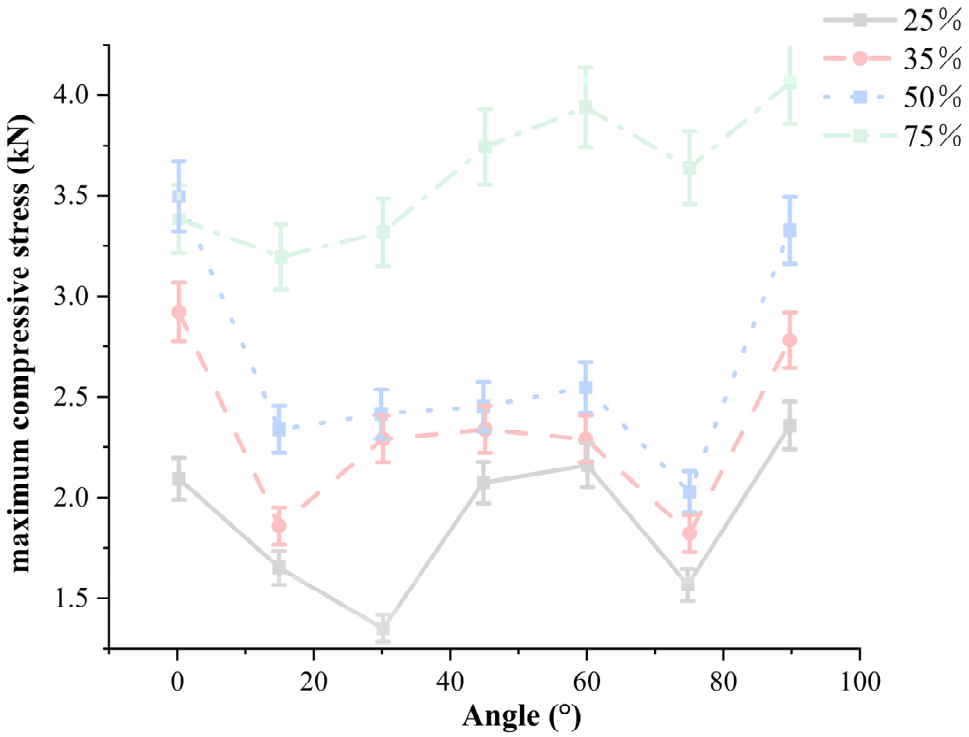


Figure 14. Variation in maximum compressive stress with printing angle for linearly filled specimens with different filling ratios.

As shown in Figure 15, the maximum compressive stress at angles ranging from 0° to 90° for honeycomb, spiral, and linear filling structures, all exhibiting a 75% filling rate. The honeycomb filling structure demonstrates significantly higher compressive stress than both the spiral and linear structures, indicating superior compressive performance among the three. At 0°, the stress reaches approximately 4.5 kN, peaking near 5.0 kN at 15° and 75°. Although stress declines at 45° and 60°, it remains greater than that of the other two structures, with corresponding error bars reflecting notable stress fluctuations. The helical filling structure displays intermediate compressive stress levels with minimal overall variation, typically maintaining values between 3.5 and 3.8 kN, and showing only a slight increase beyond 75°. In contrast, the linear filling structure exhibits the lowest overall compressive stress, indicating the weakest performance among the three. At 0°, the stress is approximately 3.4 kN, decreasing to about 3.1 kN at 15° before gradually recovering. Between 75° and 90°, it increases to around 4.0 kN, with error bars suggesting relatively stable performance. Overall, the honeycomb structure shows the highest compressive strength but with more pronounced angular fluctuations, while the linear structure presents the lowest compressive strength with more consistent performance across varying angles.

The hexagonal topology of honeycomb structures represents "nature's optimal load-bearing configuration," characterized by "uniform stress distribution across three adjacent unit edges under forces applied in any direction" (fulfilling the triaxial stress balance in the stress tensor equation). A 75% fill rate provides ample material foundation for this topology. Even when printing angles vary, hexagonal cells adapt to stress directions through geometric deformation, ensuring compressive stress remains maximized. However, at high angles (75°/90°), the force direction within hexagonal cells aligns more closely with the load-bearing edges. At low angles (15°/30°), stress must traverse layer interfaces for transfer, resulting in the greatest fluctuation amplitude.

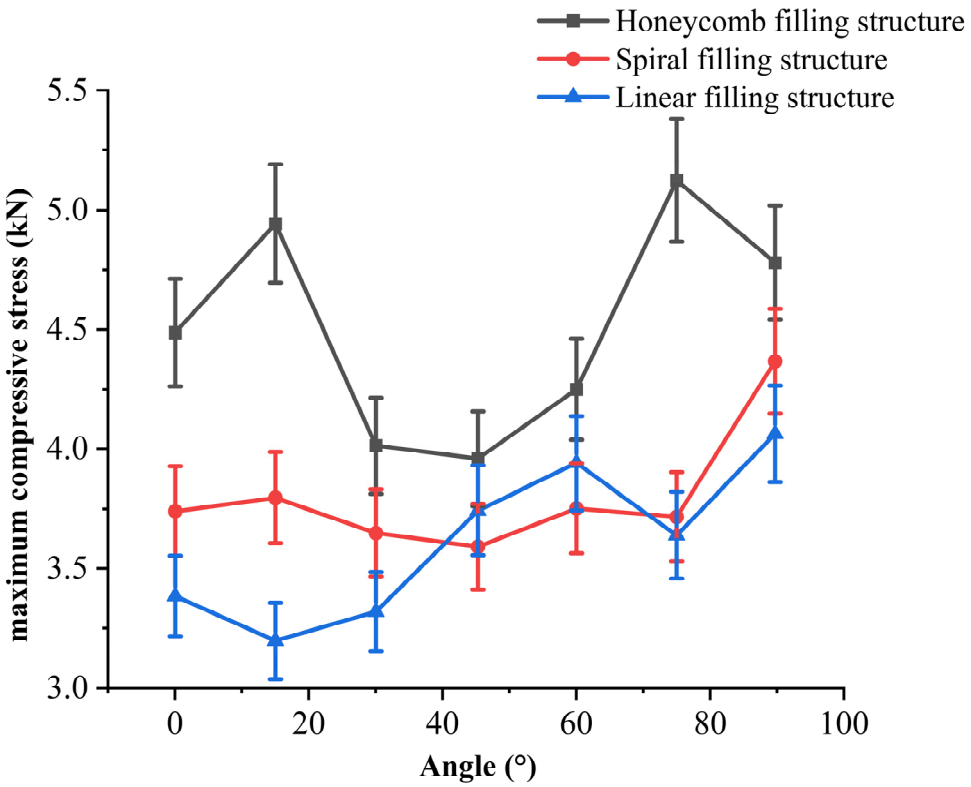


Figure 15. Compression performance curves of three different specimens as a function of printing angle at a fill rate of 75%.

The "enveloping characteristic" of helical structures confers a degree of 'isotropy'—regardless of printing angle, the helical lines form continuous load-transfer paths. This avoids the "unidirectional weakness" of linear structures while circumventing the "high angle dependency" of honeycomb structures. However, due to "tangential losses" in spiral stress transfer, the stress transmission efficiency of spiral structures is lower than that of hexagonal structures. This results in consistently lower compressive strength compared to honeycomb structures. Additionally, owing to the stability of spiral structures, their stress fluctuations exhibit smaller amplitudes than those of honeycomb structures.

Interlayer stress concentration in linear structures is a universal phenomenon across all printing angles. Regardless of angle variation, the interlayer interfaces along parallel paths remain stress weak points, resulting in the lowest overall compressive stress. Simultaneously, the issue of weak interlayer bonding persists irrespective of angle, leading to minimal performance fluctuation in linear structures and manifesting as the flattest curve.

Table 3 shows the variance of three different infill patterns when the infill method is the same, with the printing tilt angle as the only variable. Table 4 shows the variance for specimens with the infill pattern as the variable, across seven different printing tilt angles. By comparing the data, it can be intuitively seen that the variance at tilt angles of 30°, 45°, and 90° is similar to the data in Table 3. This indicates that under the conditions of 30°, 45°, and 90°, the influence of the infill pattern on the compressive performance of the specimens is similar in significance to the influence of the tilt angle on the compressive performance. However, when the printing tilt angles are 0°, 15°, and 75°, the variance in Table 4 is significantly larger than that in Table 3. This indicates that at tilt angles of 0°, 15°, and 75°, the effect of the infill pattern on the compressive performance of the specimens is significantly more pronounced than the effect of the printing tilt angle on the compressive performance.

Table 3. Maximum compressive stress variance at different angles for identical filling structures.

Filling Structure	Variance
Honeycomb	0.181
Spiral	0.067
Linear	0.128

Table 4. Maximum compressive stress variance for different filling structures at the same angle.

Angle (°)	Variance
0	0.341
15	0.791
30	0.123
45	0.063
75	0.678
90	0.143

3.2. Discussion on Existing Research

In the study conducted by Liu et al. [34], experiments were performed on five distinct specimens. The authors defined the relative density of the specimens as F_V, where a higher F_V value corresponds to increased wall thickness and, consequently, greater packing density. Their experiments produced stress–strain curves for the five specimens with differing relative densities, as shown in Figure 16. The figure clearly indicates that the specimen with a relative density of 60% exhibits the most favorable compressive performance among the five, followed by those with relative densities of 50%, 40%, 30%, and 20%, as depicted in Figure 16. Liu's findings demonstrate that specimens with higher relative densities, indicative of greater packing density, exhibit enhanced mechanical properties.

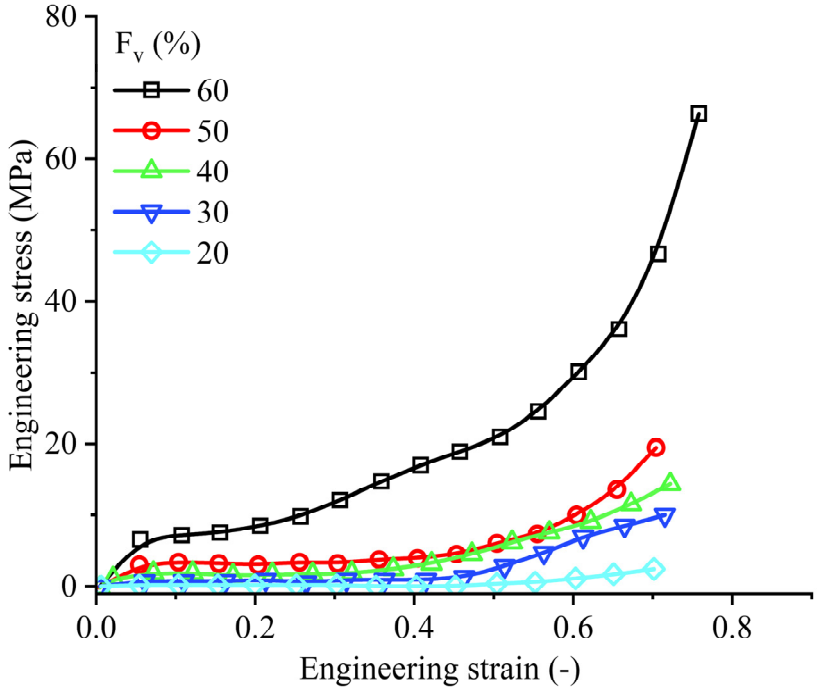


Figure 16. Stress–strain curves of specimens with different relative densities in Liu's study.

In the study by Wang et al. [35], compression tests were performed on three specimens: PDMS/PLA-3, PDMS/PLA-5, and PDMS/PLA-7. The fundamental data for these specimens are summarized in Table 5. Utilizing the same filler material, the researchers assessed the compressive properties of specimens featuring three distinct pillar diameters.

The results indicated that increasing the pillar diameter enhanced the filling rate of the specimens. The experimental data obtained by Wang et al. are illustrated in Figure 17. Their findings demonstrated that the mechanical properties of the specimens were directly affected by the pillar diameter. The specimen exhibiting the most favorable mechanical properties was the one with a 7 mm diameter, followed by the 5 mm diameter specimen. Conversely, the specimen with the least favorable mechanical properties was the 3 mm diameter specimen, as depicted in Figure 17. The study concluded that larger pillar diameters, which corresponded to higher filling rates, led to improved mechanical properties of the specimens.

Table 5. Sample labeling, filler, pillar diameter, mass, and density of PDMS/PLA lattice composites in Wang et al.'s study [35].

Specimen Label	m/g	ρ/g·cm^{-3}
PDMS/PLA-3	49.743 ± 0.142	1.066 ± 0.003
PDMS/PLA-5	50.902 ± 0.176	1.091 ± 0.004
PDMS/PLA-7	53.346 ± 0.285	1.143 ± 0.006

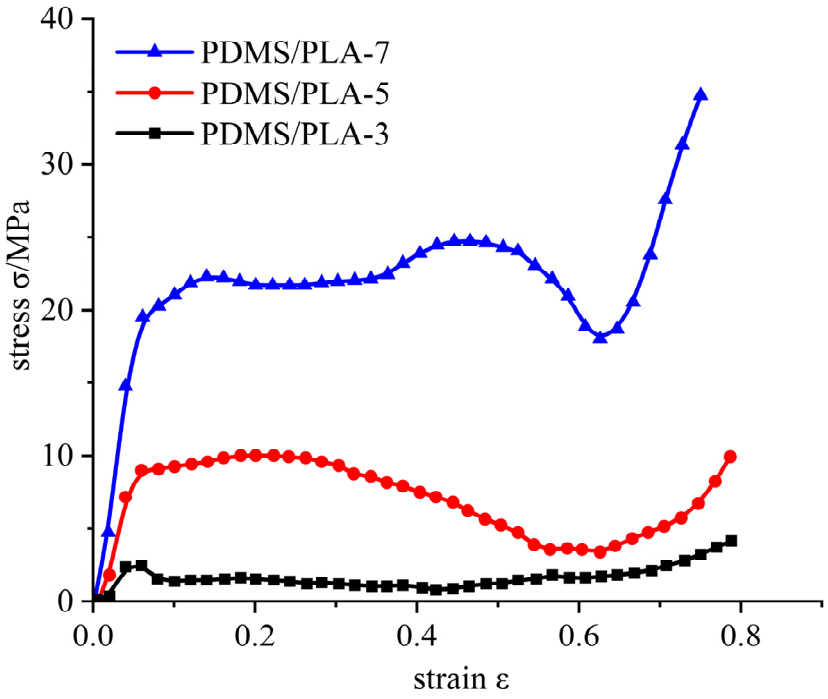


Figure 17. Stress–strain curves of different specimens in Wang's research.

In the studies conducted by Liu and Wang, the researchers modified the filling rate of components by adjusting their relative density and pillar diameter, respectively. Both Liu and Wang performed compression tests on specimens with varying filling rates. An analysis of these experiments reveals consistent conclusions: the mechanical properties of the studied samples improved as the filling rate increased. This finding is consistent with the results of the present study, which utilized different printing angles, infill patterns, and infill ratios for specimen fabrication. As shown in Figures 9–11, when both the printing angle and infill pattern were held constant, specimens with higher infill density demonstrated enhanced compressive strength.

Marine photovoltaic structures must consider not only compressive properties but also tensile and flexural characteristics. The packing ratio serves as a crucial factor that influences the compressive performance of specimens and significantly impacts their tensile and flexural properties.

Kilinc's research [36] indicates that a reduction in layer thickness and hatch spacing leads to an increase in the deposition of reinforcing fibers per unit area. The study involved the fabrication of nine specimens; for instance, "1-08" denotes a specimen with a layer thickness of 1 mm and a hatch spacing of 0.8 mm, whereas "08-06" signifies a specimen with a layer thickness of 0.8 mm and a hatch spacing of 0.6 mm. The fiber content for various specimen types is presented in Table 6.

Table 6. Fiber volume fraction of composites.

Sample Code	Fiber Content (vol%)
1-08	11.297
1-06	18.150
1-04	21.833
08-08	16.395
08-06	19.266
08-04	23.371
06-08	17.884
06-06	20.165
06-04	26.851

Kilinc et al. conducted tensile and flexural tests on nine specimens, which were categorized into three groups according to thickness (1 mm, 0.8 mm, and 0.6 mm). Each group underwent both tensile and flexural testing. As illustrated in Figures 18–23, the specimens demonstrating the highest performance in both tests across the three thickness categories were 1-04, 08-04, and 06-04, followed by 1-06, 08-06, and 06-06. The lowest-performing specimens were 1-08, 08-08, and 06-08. Their research indicated that increased fiber content, specifically higher filler loading, led to enhanced tensile and flexural strengths in the specimens.

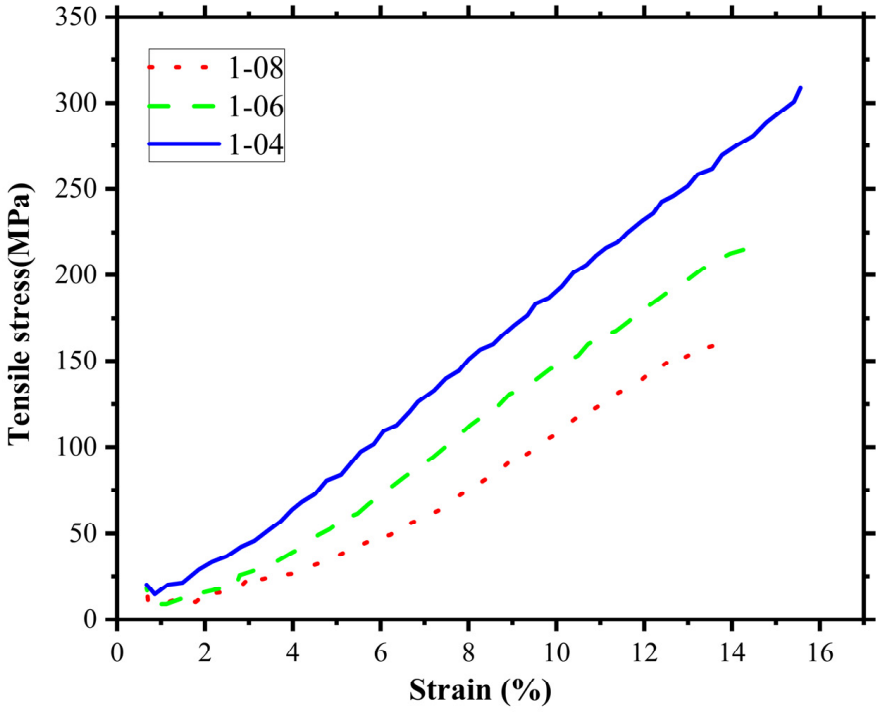


Figure 18. The stress–strain curves of specimens printed with a thickness of 1 mm and different hatch spacing values.

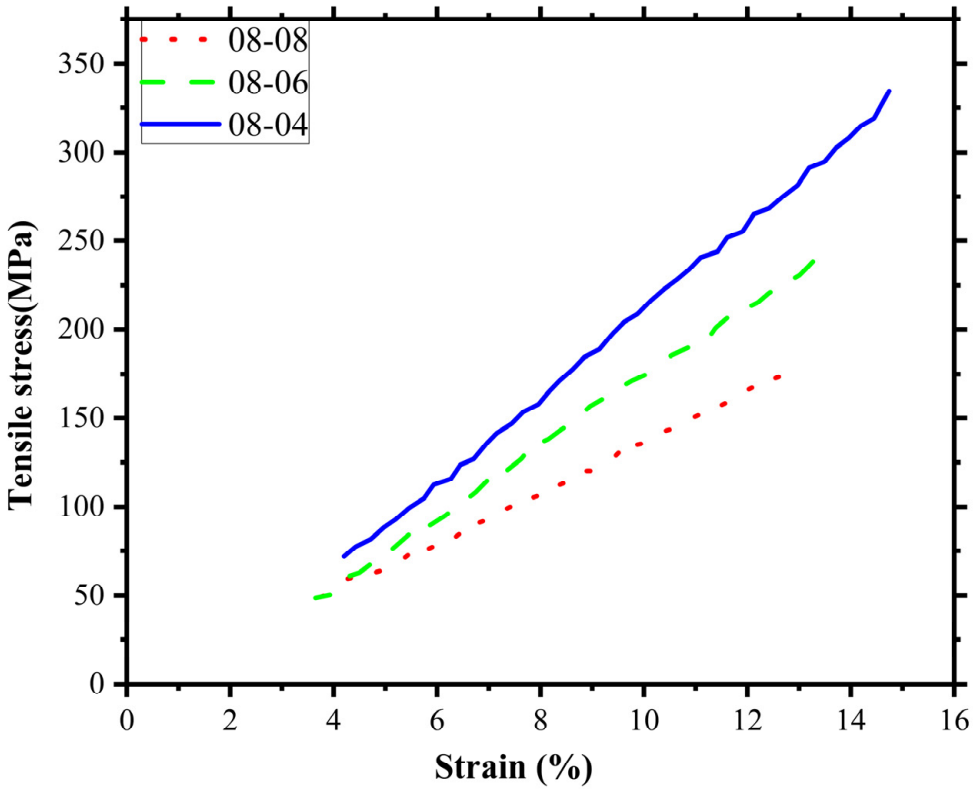


Figure 19. The stress–strain curves of specimens printed with a thickness of 0.8 mm and different hatch spacing values.

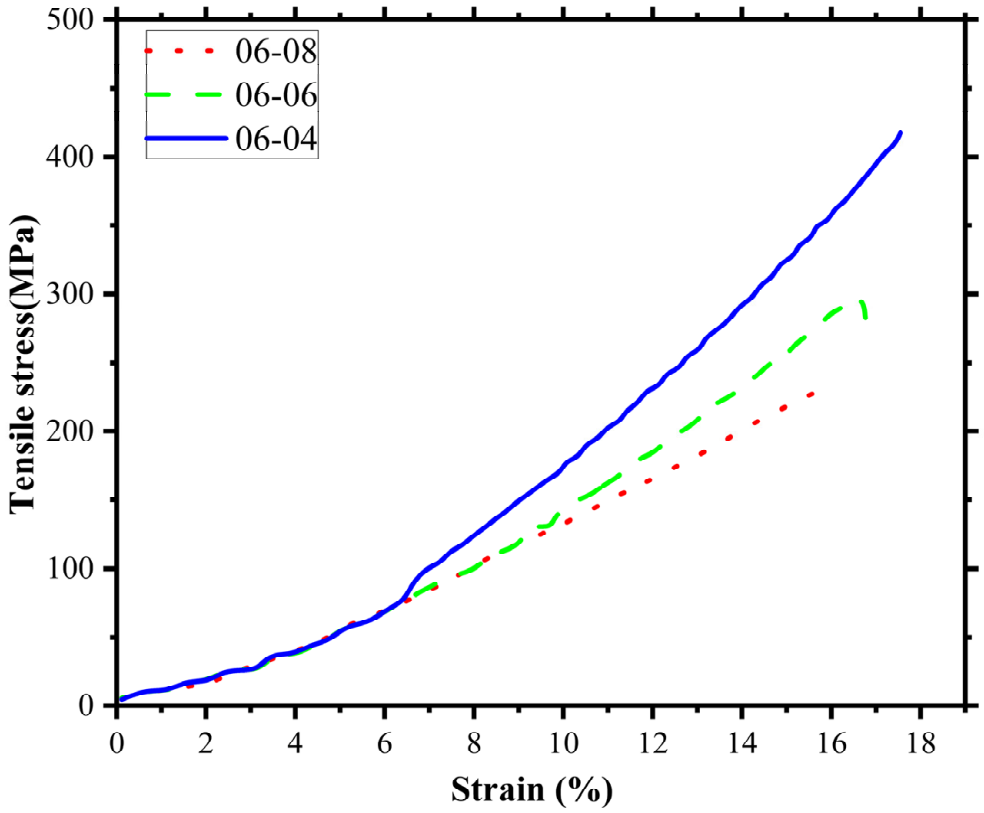


Figure 20. The stress–strain curves of specimens printed with a thickness of 0.6 mm and different hatch spacing values.

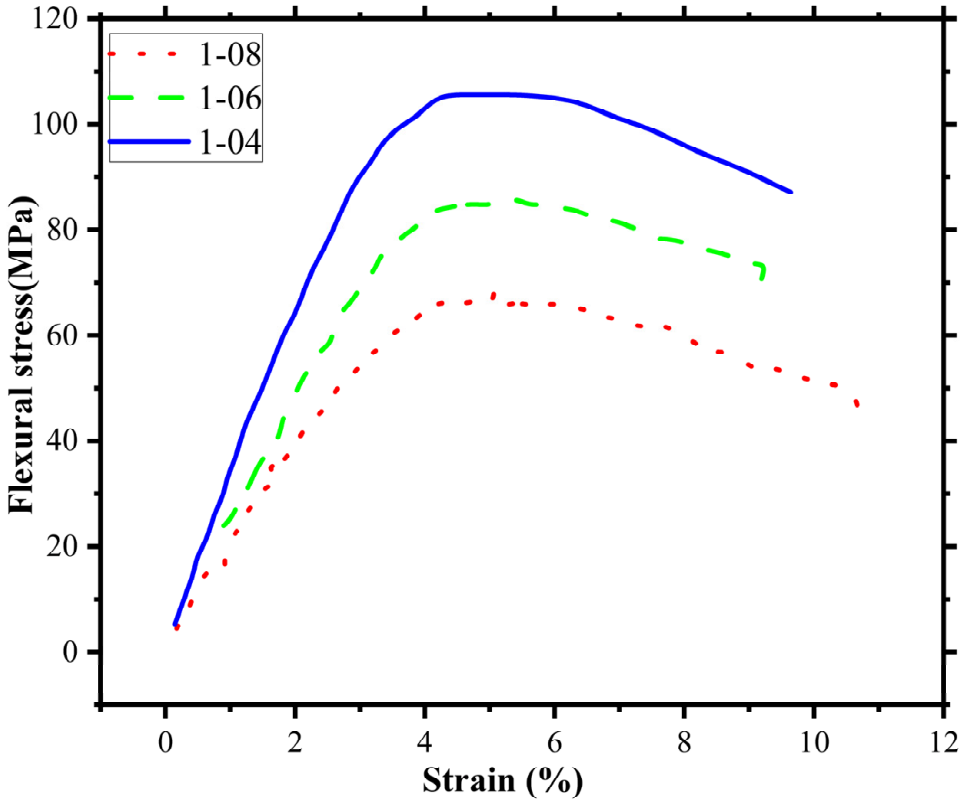


Figure 21. The flexural stress–strain curves of specimens printed with a thickness of 1 mm and different hatch spacing values.

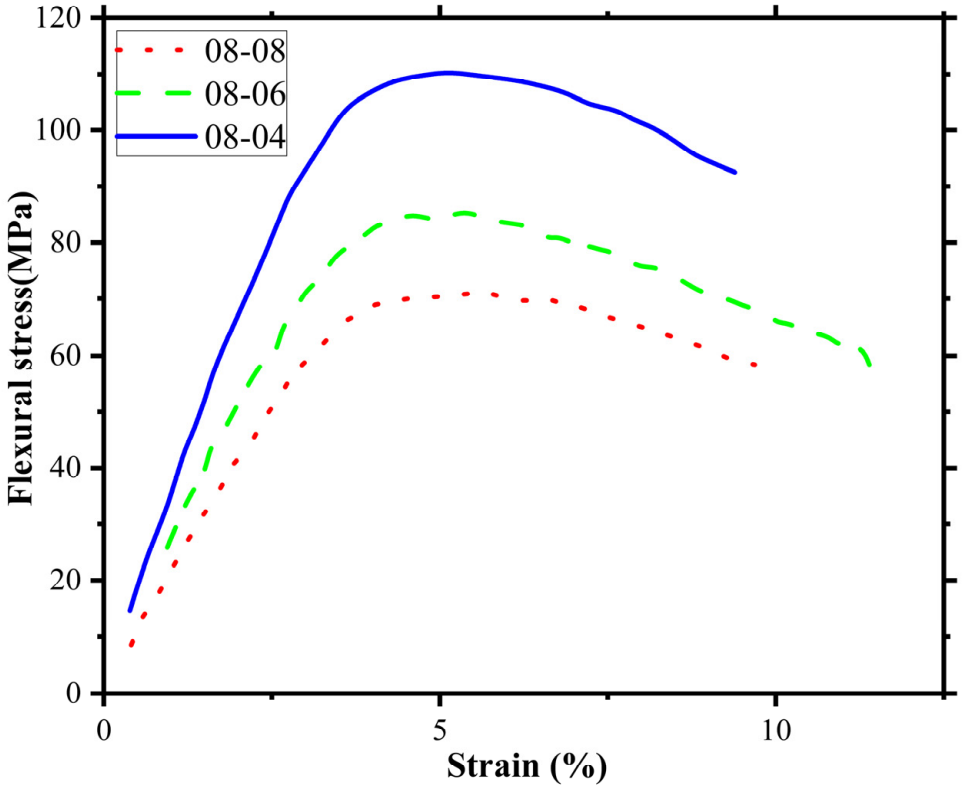


Figure 22. The flexural stress–strain curves of specimens printed with a thickness of 0.8 mm and different hatch spacing values.

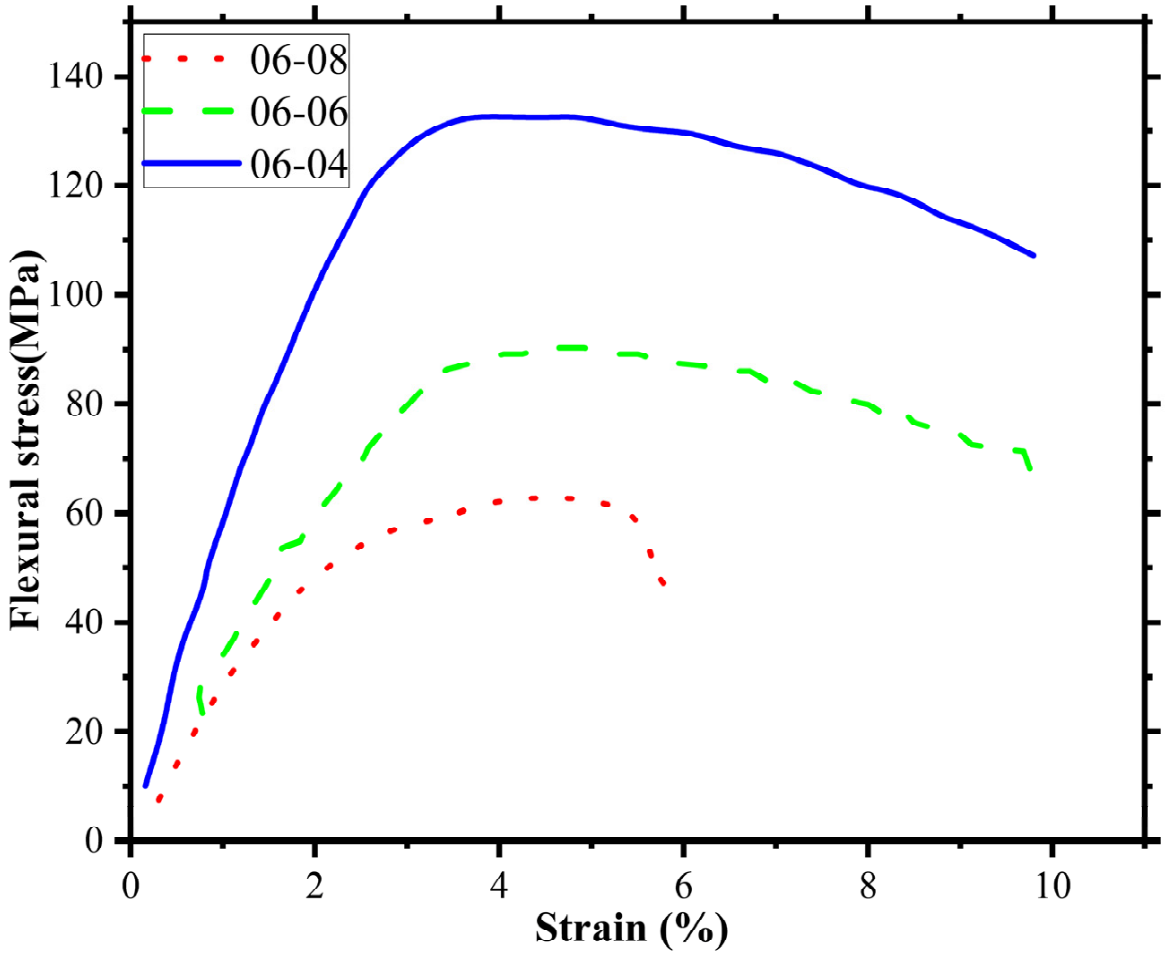


Figure 23. The flexural stress–strain curves of specimens printed with a thickness of 0.6 mm and different hatch spacing values.

The study conducted by Abdulsalam et al. [37] summarized the impact of various printing parameters on the mechanical properties of specimens, as detailed in Table 7. As the parameters increase, they influence the mechanical properties of the components, with "+" denoting an increase in response values and "-" indicating a decrease in response values.

Table 7. The Influence of Various Printing Factors on the Mechanical Properties of Test Specimens in Abdulsalam's Research.

	Tensile		Flexural		Compressive	
Printing Parameter	$F_{m,t}$, N	E_t, GPa	$F_{m,f}$, N	E_f, GPa	$F_{m,c}$, N	E_c, GPa
Infill density	+	+	+	+	+	+

The table clearly indicates that packing density is positively correlated with all three mechanical properties: compression, tensile strength, and flexural strength. Specifically, as packing density increases, the mechanical properties of the specimens also improve.

A summary of the above studies reveals that increasing the specimen filling rate significantly enhances the mechanical properties of the specimens. Integrating the experimental data yields Table 8. As mentioned earlier, this study encompasses a total of 84 data points. Twelve experiments were conducted for each of the 84 data points in this study. The average values for all data points are presented in Table 8. The table directly demonstrates that, un-

der identical conditions, the specimen with a 75% filling rate exhibits the best compressive performance among the four filling rates. Comparing the remaining three filling rates, it is also observed that the compressive performance of the specimens improves to some extent as the filling rate increases. Through the integration of data points, along with the error analysis and variance analysis of the data discussed earlier, it is not difficult to arrive at the same conclusions as those found in existing literature. This demonstrates that the research presented in this paper is reproducible and has repeatability.

Table 8. Maximum compressive stress of different specimens in this study.

		Fill Ratio			
Filling Structure	**Tilt Angle (°)**	**75%**	**50%**	**35%**	**25%**
Honeycomb	0	4.48734	4.48722	3.04724	2.15478
	15	4.94227	2.02658	0.75117	0.01473
	30	4.01366	1.77183	1.66335	0.98785
	45	3.95942	2.15478	1.73567	0.98785
	60	4.25033	2.31914	1.99042	1.26232
	75	5.12471	2.10054	1.02401	0.49642
	90	4.77956	3.7211	2.95684	2.97492
Spiral	0	3.7397	3.95683	3.42044	3.05518
	15	3.79674	2.64484	2.23357	1.86831
	30	3.64861	2.4277	2.3817	2.35962
	45	3.59157	2.53075	2.66784	2.27957
	60	3.75166	3.10118	2.67888	2.27957
	75	3.71669	2.59883	1.92536	1.6061
	90	4.36717	3.68265	2.70188	2.49579
Linear	0	3.38441	3.49737	2.92323	2.09429
	15	3.19671	2.33974	1.85903	1.65179
	30	3.31902	2.41448	2.29218	1.35028
	45	3.74283	2.4527	2.33974	2.0756
	60	3.94072	2.54698	2.29218	2.16054
	75	3.63921	2.02889	1.82166	1.56686
	90	4.06302	3.32836	2.78224	2.35843

Liu et al. verified the positive correlation between increased infill rate and improved mechanical properties by adjusting relative density, while Wang et al. explored the impact of changing pillar diameters on material mechanical performance; both findings align with the core conclusions of this study. However, these studies generally lack an in-depth exploration of the synergistic effects of multiple parameters and their application to specific scenarios. Kilinc's research focused on the effect of fiber content on tensile and bending properties, without addressing the relationship among compressive performance, infill patterns, and print angles. Although Abdulsalam et al. summarized the trends in the influence of printing parameters, they did not analyze the mechanical performance differentiation mechanism caused by differences in the topology of various infill patterns, nor did they conduct targeted analysis for the harsh environmental requirements of marine photovoltaic support structures. In contrast, this study not only systematically investigates the synergistic effects of three key parameters—fill density, infill pattern, and print angle—but also, by comparing the stress transmission paths of honeycomb, spiral, and linear infill patterns, reveals the iso-stress distribution advantage of hexagonal topologies. It clarifies the suitability of honeycomb infill at high fill density (75%) with specific print angles (75° or 90°), filling a gap in existing research regarding multi-parameter optimization and scenarios specific to marine photovoltaics. Additionally, this study verifies the significance of differences

in parameter effects through variance analysis, further deepening the understanding of the relationship between 3D printing processes and material performance. For instance, Liu et al. (2024) [34] found that specimens with a relative density (equivalent to the filling rate) of 60% exhibited optimal compressive properties. In contrast, this study demonstrates that the compressive stress of honeycomb-filled specimens continues to increase even at a filling rate of 75% (with only slight stress relaxation occurring after 50%). This discrepancy likely stems from differences in the matrix material (PLA/PHA-wood composite in Liu et al.'s study [34] versus pure PLA in this study) and the filler pattern (lattice structure in Liu et al [34]. versus honeycomb/spiral/linear fill in this study), indicating that the optimal filling rate is highly dependent on material type and topological structure. Regarding optimal printing angles, Jiang et al. (2025) [31] observed that honeycomb-filled specimens at 75% filling exhibited stable superior performance across all printing angles, aligning with the general trend in this study. However, this research further clarifies that honeycomb filling achieves peak compressive stress at 75° or 90°, whereas Jiang et al [31]. did not specify the peak angle. This refinement may stem from the finer print angle gradient employed in this study (7 angles versus fewer in Jiang et al.'s work [31]). Regarding performance gains, the maximum compressive stress (5.12 kN) achieved by honeycomb filling at 75% packing density and 75° printing angle in this study represents an approximately 28% improvement over the peak value (approximately 3.99 kN) of the lattice structure in Liu et al.'s research [34] and a roughly 12% enhancement over the performance (approximately 4.57 kN) of honeycomb filling in Jiang et al.'s study [31]. This disparity highlights the synergistic optimization effect of filling patterns, filling ratios, and printing angles—an aspect insufficiently explored in prior studies. Placing this work within a broader literature context reveals that multi-parameter synergistic optimization is a key direction for enhancing the mechanical properties of 3D-printed marine photovoltaic components. Subsequent studies on the mechanical properties of PLA-based components can reference this multi-parameter synergistic approach to optimize component performance.

Offshore photovoltaic structures are typically large in scale and must endure harsh environmental conditions, which necessitate exceptional mechanical properties in their construction. As previously noted, a higher infill density in 3D-printed specimens is associated with enhanced mechanical properties. However, beyond a certain threshold, further increases in infill density result in only marginal improvements in mechanical performance. At this juncture, alternative methods are required to improve mechanical properties, ensuring compliance with performance standards while also aiming to reduce structural mass and conserve materials. This study examines the effects of fill rate on the compressive properties of specimens, as well as the influence of printing method and angle. As shown in Figure 12, at a 75% fill rate, the honeycomb printing method consistently exhibits superior compressive performance compared to the other two methods, irrespective of the specimen's printing angle. Jiang et al. [38] utilized the same three printing methods as this study for specimen design and analysis. Compression tests were performed on specimens with a 75% fill rate. As shown, specimens featuring a honeycomb structure consistently demonstrated superior compressive performance compared to the other two structures, regardless of the printing angle, when the fill rate was maintained at 75%, as depicted in Figure 24. Jiang et al [31]. provided an explanation for this phenomenon in their research. The hexagonal topology of the honeycomb structure constitutes an 'equistress structure,' enabling uniform distribution of external forces throughout the entire structure and preventing localized stress concentration (refer to stress distribution simulation results in Jiang et al., 2025 [31]). Its interlayer bonding area is 35% larger than that of linear structures, enhancing resistance to interlaminar delamination.

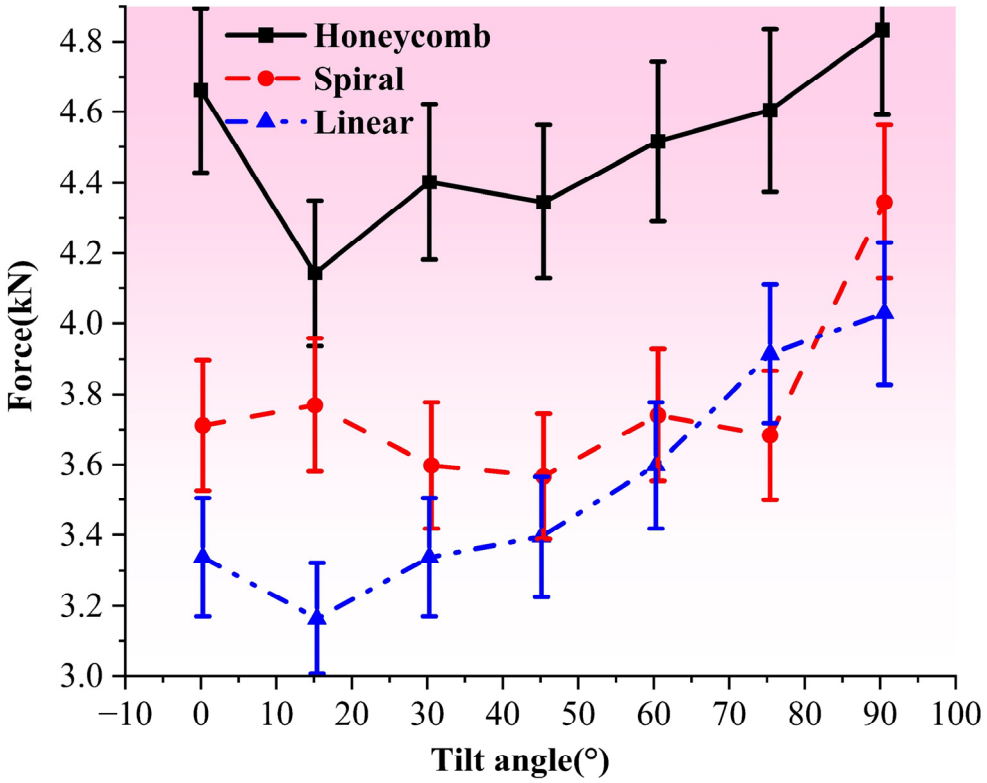


Figure 24. The compressive performance curves of three different specimens in Jiang et al.'s study [38], with the printing angle at a fill rate of 75% as the independent variable.

Although this study chose PLA as the 3D printing material and it demonstrated certain feasibility in laboratory compression performance tests, PLA, as a typical biodegradable polymer, has characteristics that make it susceptible to hydrolysis, which poses significant limitations in harsh marine environments. Under conditions of long-term immersion in seawater, high humidity, and salt spray erosion, PLA molecular chains are prone to breakage and degradation, leading to a significant decline in key mechanical properties such as compressive strength and tensile strength over service time. This makes it difficult to meet the engineering requirements of marine photovoltaic (MPV) systems, which typically need stable operation for 15–20 years. This is a core issue that this research must address at the material selection level. To address this limitation, polymers more suitable for marine environments, such as PETG, Nylon, and fiber-reinforced composites, should be included in subsequent studies and applications [38–41]. PETG has excellent hydrolysis resistance and UV aging resistance, maintaining structural stability even under fluctuations in daily marine temperatures and long-term seawater immersion, and its melt flow properties are compatible with 3D printing processes. Nylon combines high mechanical strength with seawater corrosion resistance, and its impact and fatigue resistance better respond to dynamic loads such as waves and wind. Fiber-reinforced composites (such as carbon fiber-reinforced PP and glass fiber-reinforced epoxy resin), with their high strength-to-weight ratio and excellent environmental aging resistance, have been widely used in marine engineering, with mechanical performance and environmental adaptability far exceeding that of PLA. It should be clarified that this study uses PLA as the target to explore the effects of infill pattern, density, and printing angle on compression performance. The core conclusions (such as the stress uniformity advantage of honeycomb infill and the threshold effect of high infill density) can, in principle, be transferred to optimize the 3D printing processes of the aforementioned marine-grade polymers. However, follow-up studies need to conduct targeted experiments based on the printing parameter sensitivities of different materials

(such as the printing temperature window of PETG and the pre-drying requirements of Nylon). At the same time, accelerated tests such as seawater immersion and salt spray aging should be carried out to evaluate long-term performance, so that the research conclusions better align with the actual engineering needs of MPV systems, addressing the current study's shortcomings in material environmental adaptability analysis. Furthermore, a key limitation of this study must be clarified: marine photovoltaic support structures encounter complex dynamic loads from waves, wind forces, and corrosion during actual service, rather than purely static compressive loads. Therefore, conclusions drawn solely from compression tests are insufficiently comprehensive to fully guide engineering applications. This research should be regarded as one component within the overall design framework for marine photovoltaic support structures. Regarding the potential influence of filling patterns on other critical mechanical properties: Honeycomb filling, with its stress-distribution characteristics, may enhance tensile strength and fatigue performance under cyclic loading by reducing local stress concentrations—consistent with the stress transfer mechanism observed in compression tests. In contrast, linear filling, characterized by its anisotropic structure and weak interlayer bonding, may exhibit lower tensile strength and poorer fatigue performance under cyclic tensile or bending loads due to crack propagation at interfacial interfaces. Helical filling, with its ability to resist combined bending and torsional loads, may exhibit tensile and fatigue properties intermediate between honeycomb and linear filling. However, these inferences require validation through subsequent tensile and fatigue testing to provide comprehensive mechanical performance data supporting the design of marine photovoltaic structures.

4. Conclusions

The main conclusions of this paper are as follows:

The mechanical properties of test specimens fabricated from PLA are influenced by three primary factors: infill density, printing method, and printing angle. Notably, infill density exerts the most substantial effect on the specimens. As infill density increases, the specimens demonstrate enhanced compressive properties and other mechanical characteristics.

When the infill density of a specimen attains a specific threshold, further enhancement of its mechanical properties through infill density becomes markedly constrained. At this juncture, modifying the printing method is essential to achieve improved compressive strength and other mechanical characteristics. This study unequivocally illustrates that at 75% infill density, honeycomb infill exhibits significantly superior compressive performance compared to grid or linear infill patterns.

To satisfy the mechanical performance requirements of marine photovoltaics, components are generally printed with a high infill density. In specimens exhibiting high infill density, the printing orientation has a minimal impact on improving their mechanical properties.

This study demonstrates that under laboratory testing conditions, components printed using PLA material can only meet the basic compressive strength requirements for static loading scenarios. However, the marine environment is complex and variable, subjecting structures not only to dynamic loads such as waves and wind forces but also to corrosive factors like salt spray and seawater immersion. Therefore, the specimens in this research cannot be directly applied in marine engineering. During actual service, PLA's mechanical properties (such as tensile strength, flexural strength, and fatigue performance) and chemical stability (such as hydrolysis resistance and UV aging resistance) have not been verified under real marine loading conditions. The safety margin for its long-term operation (marine photovoltaic systems require 15–20 years) remains unclear. Consequently, PLA should only be considered a potential candidate material for marine photovoltaic support

structures under specific conditions. Its practical application necessitates supplementary testing, including dynamic load testing, long-term aging tests, and safety margin calculations. Additionally, material modification—such as blending with hydrolysis-resistant polymers or incorporating reinforcing fibers—is required to further enhance its suitability for marine environments. The application of 3D printing technology and PLA materials in marine engineering necessitates a series of studies, including salinity resistance testing, high-temperature resistance testing, fatigue testing of PLA materials, and bending, torsion, and tensile tests. This represents a complex and time-consuming research process. This study tested only the compressive strength of PLA specimens under laboratory conditions. It represents a small part of the broader research exploring PLA materials for marine structures.

Author Contributions: Conceptualization, H.Z. and D.Z.; methodology, H.Z. and D.Z.; software, S.Z.; validation, S.Z. and Y.Z.; formal analysis, S.Z.; investigation, S.G.; resources, D.Z.; data curation, H.F.; writing—original draft preparation, S.Z.; writing—review and editing, D.Z.; visualization, D.Z.; supervision, D.Z.; project administration, D.Z.; funding acquisition, D.Z. All authors have read and agreed to the published version of the manuscript.

Funding: This study received no external funding.

Data Availability Statement: The original contributions presented in this study are included in the article. Further inquiries can be directed to the corresponding author.

Conflicts of Interest: The authors declare no conflicts of interest.

References

1. Pasten, C.; Santamarina, J.C. Energy and quality of life. *Energy Policy* **2012**, *49*, 468–476. [CrossRef]
2. Perez, M.; Perez, R. Update 2022—A fundamental look at supply side energy reserves for the planet. *Sol. Energy Adv.* **2022**, *2*, 100014. [CrossRef]
3. Saha, S.; Ruslan, A.R.M.; Morshed, A.K.M.M.; Hasanuzzaman, M. Global prospects and challenges of latent heat thermal energy storage: A review. *Clean Technol. Environ. Policy* **2021**, *23*, 531–559. [CrossRef]
4. Raza, M.Q.; Nadarajah, M.; Ekanayake, C. On recent advances in PV output power forecast. *Sol. Energy* **2016**, *136*, 125–144. [CrossRef]
5. Al-Ali, M.; Dincer, I. Energetic and exergetic studies of a multigenerational solar–geothermal system. *Appl. Therm. Eng.* **2014**, *71*, 16–23. [CrossRef]
6. Li, X.-Z.; Fan, X.-C.; Cheng, Z.-J. Hydropower development situation and prospects in China. *Renew. Sustain. Energy Rev.* **2018**, *82*, 232–239. [CrossRef]
7. Anderson, A.; Rezaie, B. Geothermal technology: Trends and potential role in a sustainable future. *Appl. Energy* **2019**, *248*, 18–34. [CrossRef]
8. Bilgili, F.; Koçak, E.; Bulut, Ü.; Kuşkaya, S. Can biomass energy be an efficient policy tool for sustainable development? *Renew. Sustain. Energy Rev.* **2017**, *71*, 830–845. [CrossRef]
9. Islam, M.; Mekhilef, S.; Saidur, R. Progress and recent trends of wind energy technology. *Renew. Sustain. Energy Rev.* **2013**, *21*, 456–468. [CrossRef]
10. Lv, S.; Lu, M.; Liu, W.; Li, X.; Lv, W.; Liu, Z.; Dong, X.; Lu, T.; Yang, B. Recent advances in longitudinal spatial area marine photovoltaics. *Renew. Sustain. Energy Rev.* **2025**, *208*, 115036. [CrossRef]
11. Claus, R.; López, M. Key issues in the design of floating photovoltaic structures for the marine environment. *Renew. Sustain. Energy Rev.* **2022**, *164*, 112502. [CrossRef]
12. Rosa-Clot, M.; Tina, G.M. Chapter 4—Submerged PV systems. In *Submerged and Floating Photovoltaic Systems*; Academic Press: Cambridge, MA, USA, 2018; pp. 65–87.
13. López, M.; Claus, R.; Soto, F.; Cebada, A.; Hernández-Garrastacho, Z.; Simancas, O. Structural reliability of a novel offshore floating photovoltaic system to supply energy demands of ports. In *Developments in the Analysis and Design of Marine Structures*; CRC Press: Boca Raton, FL, USA, 2021; pp. 505–512.
14. Jubayer, C.M.; Hangan, H. A numerical approach to the investigation of wind loading on an array of ground mounted solar photovoltaic (PV) panels. *J. Wind. Eng. Ind. Aerodyn.* **2016**, *153*, 60–70. [CrossRef]

15. Alrashidi, H.; Ghosh, A.; Issa, W.; Sellami, N.; Mallick, T.K.; Sundaram, S. Evaluation of solar factor using spectral analysis for CdTe photovoltaic glazing. *Mater. Lett.* **2019**, *237*, 332–335. [CrossRef]
16. *Where Sun Meets Water: Floating Solar Handbook for Practitioners*; World Bank Group: Sydney, NSW, Australia, 2019; ESMAP, SERIS.
17. Villa-Caro, R.; Carral, J.C.; Fraguela, J.Á.; López, M.; Carral, L. A review of ship mooring systems. *Brodogr. Int. J. Nav. Archit. Ocean. Eng. Res. Dev.* **2018**, *69*, 123–149. [CrossRef]
18. Huang, G.; Tang, Y.; Chen, X.; Chen, M.; Jiang, Y. A comprehensive review of floating solar plants and potentials for offshore applications. *J. Mar. Sci. Eng.* **2023**, *11*, 2064. [CrossRef]
19. Nogami, S.; Watanabe, S.; Reiser, J.; Rieth, M.; Sickinger, S.; Hasegawa, A. A review of impact properties of tungsten materials. *Fusion Eng. Des.* **2018**, *135*, 196–203. [CrossRef]
20. Xu, F.; Lin, X.; Zhou, A. Performance of internal curing materials in high-performance concrete: A review. *Constr. Build. Mater.* **2021**, *311*, 125250. [CrossRef]
21. Chen, Z.; Qiao, J.; Yang, X.; Sun, Y.; Sun, D. A review of grouting materials for pouring semi-flexible pavement: Materials, design and performance. *Constr. Build. Mater.* **2023**, *379*, 131235. [CrossRef]
22. Sun, X.; Zhong, J.; Gao, P.; Li, G.; Xiao, D.; Zhang, Z.; Gan, T. Properties of High-Performance Materials for the Crack Repair of Segment Structures. *Sustainability* **2023**, *15*, 15933. [CrossRef]
23. Bentur, A.; Mitchell, D. Material performance lessons. *Cem. Concr. Res.* **2008**, *38*, 259–272. [CrossRef]
24. Ahn, S.-J.; Lee, H.; Cho, K.-J. 3D printing with a 3D printed digital material filament for programming functional gradients. *Nat. Commun.* **2024**, *15*, 3605. [CrossRef]
25. Sun, L.; Hua, G.; Cheng, T.; Wang, Y. How to price 3D-printed products? Pricing strategy for 3D printing platforms. *Int. J. Prod. Econ.* **2020**, *226*, 107600. [CrossRef]
26. Lee, S.G.; young An, E.; Lee, J.B.; Park, J.C.; Shin, J.W.; Kim, J.K. Enhanced cell affinity of poly (d, l-lactic-co-glycolic acid)(50/50) by plasma treatment with β-(1→ 3)(1→ 6)-glucan. *Surf. Coat. Technol.* **2007**, *201*, 5128–5131. [CrossRef]
27. Ogaki, R.; Green, F.; Li, S.; Vert, M.; Alexander, M.; Gilmore, I.; Davies, M. G-SIMS of biodegradable homo-polyesters. *Appl. Surf. Sci.* **2006**, *252*, 6797–6800. [CrossRef]
28. Sasatsu, M.; Onishi, H.; Machida, Y. In vitro and in vivo characterization of nanoparticles made of MeO-PEG amine/PLA block copolymer and PLA. *Int. J. Pharm.* **2006**, *317*, 167–174. [CrossRef] [PubMed]
29. Zhao, H.; Cui, Z.; Sun, X.; Turng, L.-S.; Peng, X. Morphology and properties of injection molded solid and microcellular polylactic acid/polyhydroxybutyrate-valerate (PLA/PHBV) blends. *Ind. Eng. Chem. Res.* **2013**, *52*, 2569–2581. [CrossRef]
30. Yu, L.; Dean, K.; Li, L. Polymer blends and composites from renewable resources. *Prog. Polym. Sci.* **2006**, *31*, 576–602. [CrossRef]
31. Jiang, H.; Xie, Y.; Zeng, S.; Guo, S.; Chen, Z.; Liang, Z.; Zhang, D. Research on Lightweight Design Performance of Offshore Structures Based on 3D Printing Technology. *J. Mar. Sci. Eng.* **2025**, *13*, 2007. [CrossRef]
32. *ASTM D1621*; Standard Test Method for Compressive Properties of Rigid Cellular Plastics. American Society for Testing and Materials: New York, NY, USA, 2010.
33. Yao, T.; Deng, Z.; Zhang, K.; Li, S. A method to predict the ultimate tensile strength of 3D printing polylactic acid (PLA) materials. *Compos. Part B Eng.* **2019**, *163*, 393–402. [CrossRef]
34. Liu, T.; Zhu, J.-H.; Zhang, W.; Belhabib, S.; Guessasma, S. Microstructure and compressive behaviour of PLA/PHA-wood lattice structures processed using additive manufacturing. *Polym. Test.* **2024**, *141*, 108612. [CrossRef]
35. Wang, H.; Wang, K.; Lei, J.; Fan, X. Compressive Properties and Energy Absorption Characteristics of Co-Continuous Interlocking PDMS/PLA Lattice Composites. *Materials* **2024**, *17*, 3894. [CrossRef] [PubMed]
36. Kilinc, F.B.; Bozaci, E.; Kilinc, A.C.; Turkoglu, T. Effect of Atmospheric Plasma Treatment on Mechanical Properties of 3D-Printed Continuous Aramid Fiber/PLA Composites. *Polymers* **2025**, *17*, 397. [CrossRef]
37. Al-Tamimi, A.A.; Pandžić, A.; Kadrić, E. Investigation and prediction of tensile, flexural, and compressive properties of tough PLA material using definitive screening design. *Polymers* **2023**, *15*, 4169. [CrossRef] [PubMed]
38. El Mehtedi, M.; Buonadonna, P.; El Mohtadi, R.; Loi, G.; Aymerich, F.; Carta, M. Optimizing milling parameters for enhanced machinability of 3D-printed materials: An analysis of PLA, PETG, and carbon-fiber-reinforced PETG. *J. Manuf. Mater. Process.* **2024**, *8*, 131. [CrossRef]
39. Techawinyutham, L.; Tengsuthiwat, J.; Srisuk, R.; Techawinyutham, W.; Rangappa, S.M.; Siengchin, S. Recycled LDPE/PETG blends and HDPE/PETG blends: Mechanical, thermal, and rheological properties. *J. Mater. Res. Technol.* **2021**, *15*, 2445–2458. [CrossRef]

40. Liu, F.F.; McAuley, K.B. Improved kinetic rate constants for nylon 6, nylon 6, 6, and nylon 6/6, 6 copolymer. *Macromol. React. Eng.* **2020**, *14*, 1900037. [CrossRef]
41. Rubino, F.; Nisticò, A.; Tucci, F.; Carlone, P. Marine application of fiber reinforced composites: A review. *J. Mar. Sci. Eng.* **2020**, *8*, 26. [CrossRef]

Disclaimer/Publisher's Note: The statements, opinions and data contained in all publications are solely those of the individual author(s) and contributor(s) and not of MDPI and/or the editor(s). MDPI and/or the editor(s) disclaim responsibility for any injury to people or property resulting from any ideas, methods, instructions or products referred to in the content.